PHYSICAL REVIEW B **76**, 165108 (2007)

# Electron-phonon interaction using Wannier functions

Feliciano Giustino,* Marvin L. Cohen, and Steven G. Louie
*Department of Physics, University of California at Berkeley, Berkeley, California 94720, USA*
*and Materials Sciences Division, Lawrence Berkeley National Laboratory, Berkeley, California 94720, USA*

(Received 20 June 2007; published 4 October 2007)

We introduce a technique based on the spatial localization of electron and phonon Wannier functions to perform first-principles calculations of the electron-phonon interaction with an ultradense sampling of the Brillouin zone. After developing the basic theory, we describe the practical implementation within a density-functional framework. The proposed method is illustrated by considering a virtual crystal model of boron-doped diamond. For this test case, we first discuss the spatial localization of the electron-phonon matrix element in the Wannier representation. Then, we assess the accuracy of the Wannier-Fourier interpolation in momentum space. Finally, we study the convergence of the electron-phonon self-energies with the sampling of the Brillouin zone by calculating the electron and phonon linewidths, the Eliashberg spectral function, and the mass enhancement parameter of B-doped diamond. We show that more than $10^5$ points in the irreducible wedge of the Brillouin zone are needed to achieve convergence.

DOI: 10.1103/PhysRevB.76.165108 PACS number(s): 63.20.Kr, 71.15.−m, 74.70.−b

## I. INTRODUCTION

The electron-phonon (e-ph) interaction manifests itself in a wide range of phenomena, including the electrical resistivity, superconductivity,[1] the Kohn effect,[2] the Peierls instability,[3] and polaronic transport in organic materials.[4] In recent years, considerable attention has been drawn to the e-ph problem by photoemission experiments which revealed sharp signatures of this interaction in the quasiparticle spectra of high-temperature cuprate superconductors.[5,6] In addition, recently, the effect of the e-ph interaction in nanoscale electron transport has attracted considerable interest since there is evidence that phonon-limited carrier lifetimes might hinder the ballistic operation of carbon-based field-effect devices.[7]

The e-ph interaction has been the subject of theoretical investigations since the early attempts to explain the temperature dependence of the electrical resistivity of metals.[8] Following the pioneering investigations of Fröhlich,[9] Holstein,[10] Bardeen and Pines,[11] and later the BCS theory of superconductivity,[1] the e-ph interaction has become the prototypical example of a fermion-boson interaction and is now used as a standard benchmark for field-theoretical Green's functions methods.[12–15] Despite the continued interest in the e-ph problem, the computational methods developed so far, ranging from frozen-phonon approaches[16–18] to first-principles linear-response techniques,[19–22] still remain unpractical. As a consequence, many important aspects, such as the effects of anisotropy within the Eliashberg theory,[23,24] the validity of the Migdal theorem in the normal state,[25] and the range of validity of the Migdal-Eliashberg theory in the superconducting state,[26] remain only partially explored. In some cases, such as the Holstein polaron problem,[15] a first-principles approach has not even been attempted to the authors' knowledge. The present situation is equally unsatisfactory from the point of view of applications, since current calculations are still limited to simple systems with a few atoms per unit cell, and only very few attempts have been made to address complex systems such as carbon nanostructures,[27] doped superconductors,[28] or metallic nanowires.[29]

This situation is partly due to the significant computational burden of an e-ph calculation, which often requires a very accurate description of electron and phonon scattering processes in the proximity of the Fermi surface.[30,31]

Motivated by these considerations, we have developed a technique which makes use of Wannier functions to dramatically reduce the computational cost of an e-ph calculation. The basic idea is to exploit the localization of both electronic and lattice Wannier functions in order to compute only a limited set of electronic and vibrational states and e-ph matrix elements from first principles, and then using these results to obtain the corresponding quantities for arbitrary electron and phonon wave vectors by a generalized Fourier interpolation. In this way, it becomes possible to sample accurately the Brillouin zone at the computational cost of a standard phonon dispersion calculation.[32] Besides the significant computational advantage, the Wannier representation proves to be an ideal analytical tool for studying the e-ph interaction in terms of simplified tight-binding models (for the electrons) and force-constant models (for the phonons) while preserving the accuracy of a full first-principles calculation.

In order to illustrate our method, we present an application to boron-doped diamond. Superconductivity above liquid He temperature has recently been observed in B-doped diamond,[33] and investigations are ongoing to explore the possibility of increasing $T_c$ beyond 10 K by tuning sample preparation and doping treatments.[34] Previous theoretical works showed that superconductivity in diamond is crucially linked to the presence of the B atoms.[28,35] Boron provides both the hole carriers participating in the supercurrent and the localized vibrations of the $BC_4$ tetrahedra responsible for the pairing field. To keep the focus on the methodology, in the present work, we prefer to adopt a simplified point of view, and we describe B-doped diamond by a virtual crystal model.[36,37]

The present paper is organized as follows. In Sec. II, we review the current techniques to compute the electron and

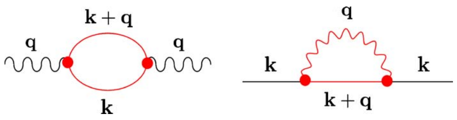

FIG. 1. (Color online) First-order e-ph diagrams considered in this work (red). Left: the self-energy of a phonon with momentum **q** (black wiggly line) is given by the Fermion loop containing two electron lines (red lines) connected by the bare e-ph vertices (red disks) (Refs. 1 and 12). Right: the self-energy of an electron with momentum **k** (black straight line) is given by the loop with one electron line (straight) and one phonon line (wiggly), connected by the bare e-ph vertices. Equations (1) and (2) were obtained from these diagrams.

phonon self-energies arising from the e-ph interaction. In Sec. III, we introduce the electron and phonon Wannier functions and derive the e-ph matrix element in the Wannier representation. Section IV describes the generalized Wannier-Fourier interpolation of the e-ph matrix element and its practical implementation within a density-functional framework. In Sec. VI, we illustrate the theory by calculating the electron and phonon linewidths, the Eliashberg function, and the electron-phonon mass enhancement parameter of boron-doped diamond.

The present work extends and improves upon the method proposed in Ref. 35. In particular, in the present work, the electron and phonon coordinates are treated on the same footing, leading to a joint electron-phonon Wannier representation and a simultaneous electron-phonon Fourier interpolation. In the Appendix, we establish the connection with the procedure outlined in Ref. 35, and we discuss the relative merits of the two strategies.

## II. ELECTRON-PHONON INTERACTION

The formalism for addressing the e-ph interaction has been set by the seminal contributions of Fröhlich,[9] Bardeen and Pines,[11] and Engelsberg and Schrieffer.[38] The e-ph Hamiltonian derived in these studies is conveniently dealt with by standard Green's functions techniques.[1,14] The interacting electron and phonon propagators are, in principle, fully determined through Dyson's equation once the corresponding electron ($\Sigma$) and phonon ($\Pi$) self-energy operators associated with the mutual interactions are known. Instead of reviewing the possible approximations to the self-energy operators, we focus here on the simplest one, which consists in replacing the dressed e-ph vertex $\Gamma$ by its bare counterpart $g$ (Fig. 1).[1] This approximation is connected with the Born-Oppenheimer adiabatic theorem and is generally referred to as the Migdal approximation.[25,26] In this work, we replace the dressed electron Green's function by the corresponding free propagator, thereby avoiding complications associated with self-consistency. On the other hand, the fully renormalized phonon frequencies, as obtained from density-functional calculations, will be adopted in the phonon propagator. This is generally considered to be a sensible approximation.[14]

The electron and phonon self-energies arising from the e-ph interaction (Fig. 1) read[12]

$$\Sigma = i \int \frac{d2}{(2\pi)^4} |g(1,2)|^2 D(1-2) G_0(2), \tag{1}$$

$$\Pi = -2i \int \frac{d1}{(2\pi)^4} |g(1,2)|^2 G_0(1) G_0(2), \tag{2}$$

where $G_0$ and $D$ are the bare electron and the dressed phonon Green's functions, respectively, $1=(\mathbf{k},\omega)$ the quadrimomentum in compressed notation ($\mathbf{k}$ being the wave vector and $\omega$ the energy), and $g(1,2)$ the electron-phonon matrix element.[39] Equations (1) and (2) were originally derived for the electron gas and need to be rewritten within the reduced-zone scheme for a practical calculation.

We make the following approximations: (i) we neglect the changes in the electronic wave functions and phonon eigendisplacements arising from the e-ph interaction,[40] (ii) we take the expectation value of the self-energy operators on the noninteracting electron and phonon states, and (iii) we restrict our discussion to the imaginary parts of the electron ($\Sigma''$) and phonon ($\Pi''$) self-energies, i.e., we only consider the corresponding linewidths. These simplifications are intended to illustrate our methodology by focusing on a few specific cases. The inclusion of the off-diagonal corrections and the calculation of the corresponding real self-energies are both feasible and will be the subject of a future communication.[41] By expressing the free propagators in terms of the noninteracting electronic energy $\epsilon_{n\mathbf{k}}$ (with $n$ the band index and $\mathbf{k}$ the momentum) and vibrational frequency $\omega_{\mathbf{q}\nu}$ (with $\nu$ the branch index and $\mathbf{q}$ the momentum), Eqs. (1) and (2) can be integrated analytically to yield[12]

$$\begin{aligned}\Sigma''_{n\mathbf{k}} = \pi \sum_{m\nu} \int_{\mathrm{BZ}} \frac{d\mathbf{q}}{\Omega_{\mathrm{BZ}}} |g^{\mathrm{SE}}_{mn,\nu}(\mathbf{k},\mathbf{q})|^2 \\ \times [(n_{\mathbf{q}\nu} + f_{m\mathbf{k+q}}) \delta(\epsilon_{n\mathbf{k}} - \omega_{\mathbf{q}\nu} - \epsilon_{m\mathbf{k+q}}) \\ + (n_{\mathbf{q}\nu} + 1 - f_{m\mathbf{k+q}}) \delta(\epsilon_{n\mathbf{k}} + \omega_{\mathbf{q}\nu} - \epsilon_{m\mathbf{k+q}})],\end{aligned} \tag{3}$$

$$\begin{aligned}\Pi''_{\mathbf{q}\nu} = 2\pi \sum_{mn} \int_{\mathrm{BZ}} \frac{d\mathbf{k}}{\Omega_{\mathrm{BZ}}} |g^{\mathrm{SE}}_{mn,\nu}(\mathbf{k},\mathbf{q})|^2 \\ \times (f_{n\mathbf{k}} - f_{m\mathbf{k+q}}) \delta(\omega_{\mathbf{q}\nu} + \epsilon_{n\mathbf{k}} - \epsilon_{m\mathbf{k+q}}),\end{aligned} \tag{4}$$

where $f_{n\mathbf{k}}$ and $n_{\mathbf{q}\nu}$ are the Fermi-Dirac and Bose-Einstein occupations, respectively, the factor of 2 accounts for the spin degeneracy, and the integrations extend over the Brillouin zone. The e-ph matrix element (vertex) $g^{\mathrm{SE}}_{mn,\nu}(\mathbf{k},\mathbf{q})$ appearing in Eqs. (3) and (4) is given by

$$g^{\mathrm{SE}}_{mn,\nu}(\mathbf{k},\mathbf{q}) = \left(\frac{\hbar}{2m_0\omega_{\mathbf{q}\nu}}\right)^{1/2} g_{mn,\nu}(\mathbf{k},\mathbf{q}), \tag{5}$$

where $m_0$ is a convenient reference mass, and

$$g_{mn,\nu}(\mathbf{k},\mathbf{q}) = \langle m\mathbf{k}+\mathbf{q}|\partial_{\mathbf{q}\nu}V|n\mathbf{k}\rangle. \tag{6}$$

We adopt the superscript "SE" to distinguish between the matrix element appearing in the self-energy expressions ($g^{\mathrm{SE}}$, with the dimensions of an energy) and the one used in the Bloch to Wannier transformation ($g$, with dimensions of an energy divided by a length, cf. Sec. III). In Eq. (6), $|n\mathbf{k}\rangle$ and

$|m\mathbf{k}+\mathbf{q}\rangle$ indicate Bloch eigenstates, while the operator $\partial_{\mathbf{q}\nu}V$ is the derivative of the self-consistent potential with respect to a collective ionic displacement corresponding to a phonon with branch index $\nu$ and momentum $\mathbf{q}$ (cf. Sec. III).[42]

Within the isotropic approximation to Eliashberg theory,[26] the phonon linewidths [Eq. (4)] constitute a key ingredient for calculating the Eliashberg function $\alpha^2F$ and the associated mass enhancement parameter λ (Ref. 43):

$$\alpha^2F(\omega) = -\frac{1}{\pi N_F}\sum_\nu \int_{\mathrm{BZ}} \frac{d\mathbf{q}}{\Omega_{\mathrm{BZ}}} \frac{\Pi''_{\mathbf{q}\nu}}{\omega_{\mathbf{q}\nu}} \delta(\omega-\omega_{\mathbf{q}\nu}), \tag{7}$$

$$\lambda = 2\int_0^\infty d\omega\omega^{-1}\alpha^2F(\omega), \tag{8}$$

$N_F$ being the density of electronic states at the Fermi level. The mass enhancement parameter λ is also referred to as the electron-phonon coupling strength and is widely used to estimate the transition temperature of conventional superconductors by means of the semiempirical McMillan formula.[44]

Inspection of Eq. (4) reveals that the calculation of the phonon linewidths requires a summation over electronic transitions where both the initial state $|n\mathbf{k}\rangle$ and the final state $|m\mathbf{k}+\mathbf{q}\rangle$ are pinned close to the Fermi level by the selection rule $\epsilon_{m\mathbf{k}+\mathbf{q}}=\epsilon_{n\mathbf{k}}+\omega_{\mathbf{q}\nu}$. As a consequence, the calculation of vibrational linewidths requires a determination of the initial and final electronic states, the phonon states of interest, and the associated e-ph matrix elements with fine energy and momentum resolutions. Whereas total-energy calculations for metals usually require at most a few tens of $\mathbf{k}$ points in the irreducible wedge of the Brillouin zone, in the present case, a much denser sampling is required to achieve numerical convergence, even up to several millions of $\mathbf{k}$ points.[30,45,46]

Similar considerations apply to the calculations of the electron self-energy [Eq. (3)], to the Eliashberg function [Eq. (7)], and to the mass enhancement parameter [Eq. (8)]. In particular, the difficulty in the determination of the mass enhancement parameter translates into a large uncertainty in the calculated superconducting transition temperature through the McMillan equation.[35] Even within more sophisticated approaches where superconducting properties are determined directly from first principles,[47] the practical implementations suffer from a strong sensitivity to the sampling of e-ph scattering processes near the Fermi surface.[31] In the following sections, we describe how it is possible to circumvent such difficulties by reformulating the e-ph vertex in the Wannier representation.

## III. ELECTRON-PHONON VERTEX IN THE WANNIER REPRESENTATION

In this section, we introduce the Wannier representation of the e-ph vertex. We first describe the electronic Wannier functions and the phonon perturbation potential in the Wannier representation. Then, we derive the relation between the e-ph matrix elements in the Wannier representation and those in the Bloch representation.

### A. Electronic Wannier functions

Wannier functions were first introduced to study the excitonic levels of polar insulators using a localized representation.[48] In the most general case, the relation between the Bloch functions $\psi_{n\mathbf{k}}(\mathbf{r})=\langle\mathbf{r}|n\mathbf{k}\rangle$ and the Wannier functions $w_m(\mathbf{r}-\mathbf{R}_e)=\langle\mathbf{r}|m\mathbf{R}_e\rangle$ is given by a Fourier transform in the momentum ($\mathbf{k}$) and lattice vector ($\mathbf{R}_e$) variables, generalized to include band mixing:[49]

$$|m\mathbf{R}_e\rangle = \sum_{n\mathbf{k}} e^{-i\mathbf{k}\cdot\mathbf{R}_e} U_{nm,\mathbf{k}} |n\mathbf{k}\rangle. \tag{9}$$

Whenever the mixing matrix $U_{nm,\mathbf{k}}$ is unitary, the Wannier states turn out to be orthonormal: $\langle m'\mathbf{R}'_e|m\mathbf{R}_e\rangle = \delta(\mathbf{R}_e,\mathbf{R}'_e)\delta(m,m')$. The inverse relation of Eq. (9) is obtained by a standard inverse Fourier transform:

$$|n\mathbf{k}\rangle = \frac{1}{N_e}\sum_{m\mathbf{R}_e} e^{i\mathbf{k}\cdot\mathbf{R}_e} U^\dagger_{mn,\mathbf{k}} |m\mathbf{R}_e\rangle. \tag{10}$$

We consider here a periodic lattice which is a supercell of the primitive cell of the crystal. Accordingly, we use discrete summations in Eqs. (9) and (10) instead of integrals over continuous variables. The expressions we derive are therefore ready to be implemented in existing computational schemes. In going from Eq. (9) to Eq. (10), we used the relation $\Sigma_{\mathbf{k}} \exp[i(\mathbf{k}-\mathbf{k}')\cdot\mathbf{R}_e]=N_e\delta(\mathbf{k},\mathbf{k}')$, where $N_e$ is the number of unit cells in the supercell, corresponding to the number of $\mathbf{k}$ points included in the calculation.

The usefulness of the Wannier representation relies on the spatial localization of the electronic states. Equation (9) indicates a large freedom associated with the transformation from Bloch to Wannier functions, since one has to choose both the manifold of the initial Bloch states and the unitary rotation associated with such a manifold. When the system under consideration presents a composite set of bands isolated from other bands by finite energy gaps, the choice of the Bloch manifold is natural and it remains to choose the unitary transform $U_{nm,\mathbf{k}}$. The most convenient choice for the purposes of the present work is the one leading to *maximally localized Wannier functions*.[49] In this case, the unitary transform is determined by requiring that the resulting Wannier functions minimize the Berry-phase spatial spread operator defined within the framework of the modern theory of polarization.[49–51] Wannier functions determined according to this procedure exhibit exponential localization.[52]

In the case of metals, the relevant bands do not usually constitute a composite manifold, and the previous procedure cannot be applied directly. Nonetheless, a *disentanglement* strategy, which allows the extraction of an optimally connected subspace from an initial entangled manifold, has already been introduced and demonstrated for simple metals.[53] This procedure consists at projecting the electronic Hamiltonian onto an appropriate subspace to treat a metallic system in effectively the same way as a hole-doped insulator. This technique is currently in use for transport problems.[54]

### B. Phonon perturbation in the Wannier representation

The potential $V(\mathbf{r})$ appearing in the e-ph matrix element [Eq. (6)] includes both the ionic contribution and the electronic self-consistent field. Within linear-response theory, this potential can be formally obtained by screening the bare ionic potentials $V_\kappa^{\text{ion}}(\mathbf{r})$ with the electronic dielectric function taken in the static limit $\epsilon(\mathbf{r},\mathbf{r}')$ (Ref. 42):

$$V(\mathbf{r};\{\boldsymbol{\tau}_{\kappa p}\}) = \int d\mathbf{r}'\,\epsilon^{-1}(\mathbf{r},\mathbf{r}') \sum_{\kappa,\mathbf{R}_p} V_\kappa^{\text{ion}}(\mathbf{r}' - \boldsymbol{\tau}_{\kappa p}). \tag{11}$$

In Eq. (11), the sum extends over all the unit cells of the crystal centered at the lattice vectors $\mathbf{R}_p$ and over all the atoms $\kappa$ located at the sites $\boldsymbol{\tau}_\kappa$ within each unit cell. The absolute coordinate of each ion is $\boldsymbol{\tau}_{\kappa p} \equiv \mathbf{R}_p + \boldsymbol{\tau}_\kappa$. $\{\boldsymbol{\tau}_{\kappa p}\}$ indicates all the ionic coordinates in the crystal. In a pseudopotential calculation, the core electrons are assumed to follow rigidly the corresponding ions, and the potentials $V_\kappa^{\text{ion}}(\mathbf{r})$ in Eq. (11) need to be replaced by the ionic pseudopotentials. The extension of the formalism to nonlocal pseudopotentials does not pose any problem provided that the nonlocality is short ranged. The variation $\partial_{\mathbf{q}\nu}V(\mathbf{r})$ of the self-consistent potential with respect to a collective ionic displacement $\Delta\boldsymbol{\tau}_{\kappa p}^{\mathbf{q}\nu}$ corresponding to a phonon with momentum $\mathbf{q}$ and branch index $\nu$ is obtained from

$$\partial_{\mathbf{q}\nu}V(\mathbf{r}) = \frac{\partial}{\partial\eta} V(\mathbf{r};\{\boldsymbol{\tau}_{\kappa p} + \eta\Delta\boldsymbol{\tau}_{\kappa p}^{\mathbf{q}\nu}\}). \tag{12}$$

Denoting the vibrational eigenmodes by $\langle\boldsymbol{\tau}_{\kappa p}|\mathbf{q}\nu\rangle = e^{i\mathbf{q}\cdot\mathbf{R}_p}\mathbf{e}_{\mathbf{q}\kappa}^{\nu}$, with $\mathbf{e}_{\mathbf{q}\kappa}^{\nu}$ cell periodic and normalized, and the ionic masses by $m_\kappa$, we can express the displacements in Eq. (12) as follows:[42]

$$\Delta\boldsymbol{\tau}_{\kappa p}^{\mathbf{q}\nu} = \text{Re}\left[\left(\frac{m_0}{m_\kappa}\right)^{1/2} \mathbf{e}_{\mathbf{q}\kappa}^{\nu} e^{i\mathbf{q}\cdot\mathbf{R}_p}\right]. \tag{13}$$

Before transforming the phonon perturbation $\partial_{\mathbf{q}\nu}V(\mathbf{r})$ [Eq. (12)] in the Wannier representation, it is instructive to rewrite the vibrational eigenmodes in a form similar to Eq. (10):

$$\langle\boldsymbol{\tau}_{\kappa p}|\mathbf{q}\nu\rangle = \sum_{\kappa'\mathbf{R}'_p} e^{i\mathbf{q}\cdot\mathbf{R}'_p}\mathbf{e}_{\mathbf{q}\kappa'}^{\nu}\,\delta(\boldsymbol{\tau}_{\kappa p} - \boldsymbol{\tau}_{\kappa' p'}). \tag{14}$$

By comparing Eqs. (14) and (10), we realize that (i) the maximally localized Wannier functions for vibrational modes (*lattice Wannier functions*) correspond to the displacement of individual ions $\delta(\boldsymbol{\tau}_{\kappa p} - \boldsymbol{\tau}_{\kappa' p'})$ and (ii) the cell-periodic part of the vibrational eigenmode $\mathbf{e}_{\mathbf{q}\kappa}^{\nu}$ for the phonons plays a role analogous to that of the unitary transformation $U_{mn,\mathbf{k}}$ for the electrons. This aspect was first pointed out in a study of lattice Wannier functions for the linear harmonic chain[55] and subsequently verified by explicitly constructing maximally localized phonon Wannier functions in a three-dimensional system.[56] The fact that extreme localization is achievable in the case of lattice vibrations relates to the discrete number of degrees of freedom associated with the classical ions.

By combining Eqs. (11)–(13), we can express the variation of the self-consistent potential $\partial_{\mathbf{q}\nu}V(\mathbf{r})$ in terms of the contributions arising from each individual ion:

$$\partial_{\mathbf{q}\nu}V(\mathbf{r}) = \text{Re}\left[\sum_{\kappa,\mathbf{R}_p} e^{i\mathbf{q}\cdot\mathbf{R}_p}\left(\frac{m_0}{m_\kappa}\right)^{1/2} \mathbf{e}_{\mathbf{q}\kappa}^{\nu}\cdot\partial_{\kappa,\mathbf{R}_p}V(\mathbf{r})\right], \tag{15}$$

where the real-valued vector field

$$\partial_{\kappa,\mathbf{R}_p}V(\mathbf{r}) = \nabla_{\boldsymbol{\tau}_{\kappa p}} V(\mathbf{r};\{\boldsymbol{\tau}_{\kappa' p'}\}) \tag{16}$$

represents the gradient of the self-consistent potential with respect to the displacement of the ion $\kappa$ in the unit cell $\mathbf{R}_p$. Following the preceding discussion about Eq. (14), it is natural to call $\partial_{\kappa,\mathbf{R}_p}V(\mathbf{r})$ the *phonon perturbation in the Wannier representation.* For practical purposes, it is convenient to introduce the displacement field $\mathbf{u}_{\mathbf{q}\kappa}^{\nu} = (m_0/m_\kappa)^{1/2}\mathbf{e}_{\mathbf{q}\kappa}^{\nu}$ and to redefine $\partial_{\mathbf{q}\nu}V(\mathbf{r})$ as the complex scalar field:

$$\partial_{\mathbf{q}\nu}V(\mathbf{r}) = \sum_{\kappa,\mathbf{R}_p} e^{i\mathbf{q}\cdot\mathbf{R}_p}\mathbf{u}_{\mathbf{q}\kappa}^{\nu}\cdot\partial_{\kappa,\mathbf{R}_p}V(\mathbf{r}), \tag{17}$$

keeping in mind that the real-valued field in the right-hand side of Eq. (12) is obtained through $\frac{1}{2}[\partial_{\mathbf{q}\nu}V(\mathbf{r}) + \partial_{-\mathbf{q}\nu}V(\mathbf{r})]$.[57] By inverting Eq. (17), we obtain

$$\partial_{\kappa,\mathbf{R}_p}V(\mathbf{r}) = \frac{1}{N_p}\sum_{\mathbf{q}\nu} e^{-i\mathbf{q}\cdot\mathbf{R}_p}[\mathbf{u}_{\mathbf{q}\kappa}^{\nu}]^{-1}\partial_{\mathbf{q}\nu}V(\mathbf{r}), \tag{18}$$

with $N_p$ being the number of unit cells in the periodic supercell considered for the lattice dynamics. In principle, $N_p$ can differ from the corresponding number of unit cells $N_e$ for the electrons in Eq. (10).

For our purposes, it is crucial that the phonon perturbation [Eq. (18)] be localized in real space. From a qualitative point of view, $\partial_{\kappa,\mathbf{R}_p}V(\mathbf{r})$ represents the potential associated with a screened dipole. In a metallic system, and within a simple Thomas-Fermi approximation, a potential of this kind would decay with the distance $r$ as $(\mathbf{r}\cdot\Delta\boldsymbol{\tau}_{\kappa p})r^{-2}\exp(-r/\lambda_{\text{TF}})$, with $\lambda_{\text{TF}}$ being the Thomas-Fermi screening length. In an insulating system, the incomplete screening makes the screened dipole decay at large distances as $Z_B r^{-2}$, with $Z_B$ being the Born dynamical charge associated with the displaced ion. Whenever the dynamical charges are nonvanishing (as is the case in polar insulators), the long-range component of the perturbation needs to be treated separately.

A quantitative assessment of the spatial localization of $\partial_{\kappa,\mathbf{R}_p}V(\mathbf{r})$ can be formulated by making connection with the spatial decay of the interatomic force constants $C(\boldsymbol{\tau}_{\kappa p},\boldsymbol{\tau}_{\kappa' p'}) = \nabla_{\boldsymbol{\tau}_{\kappa p}}\mathbf{F}(\boldsymbol{\tau}_{\kappa' p'})$, with $\mathbf{F}(\boldsymbol{\tau}_{\kappa' p'})$ the Hellmann-Feynman force acting on the ion $\kappa'$ in the unit cell $\mathbf{R}'_p$. To this end, we temporarily ignore the exchange-correlation contribution $v_{\text{xc}}$ to the self-consistent potential $V(\mathbf{r})$ and consider the electrostatic component including the Hartree and the ionic term: $V_{\text{es}}(\mathbf{r}) = V_{\text{Ha}}(\mathbf{r}) + V_{\text{ion}}(\mathbf{r}) = V(\mathbf{r}) - v_{\text{xc}}(\mathbf{r})$. By evaluating $\partial_{\kappa,\mathbf{R}_p}V_{\text{es}}(\mathbf{r})$ at $\mathbf{r} = \boldsymbol{\tau}_{\kappa' p'}$, we obtain the change of the potential experienced by the atom at $\boldsymbol{\tau}_{\kappa' p'}$ due to a displacement of the atom at $\boldsymbol{\tau}_{\kappa p}$. The gradient of this quantity with respect to $\boldsymbol{\tau}_{\kappa' p'}$ is by definition the force acting on the ion located at $\boldsymbol{\tau}_{\kappa' p'}$ [cf. Eqs. (8) and (13) of Ref. 32]. As a consequence, the following relation holds between the phonon perturbation in the Wannier representation and the matrix of the interatomic force constants:

$$\nabla_{\mathbf{r}}[\partial_{\kappa,\mathbf{R}_p} V_{\mathrm{es}}(\mathbf{r})]_{\mathbf{r}=\boldsymbol{\tau}_{\kappa' p'}} = Z_{\kappa'} C(\boldsymbol{\tau}_{\kappa p}, \boldsymbol{\tau}_{\kappa' p'}), \tag{19}$$

with $Z_{\kappa'}$ being the electric charge of the ionic species $\kappa'$. If the system under consideration can be described by the local-density approximation to density-functional theory, the exchange-correlation contribution to the self-consistent potential is short ranged, and $\partial_{\kappa,\mathbf{R}_p} V(\mathbf{r})$ decays within the same distance as $\partial_{\kappa,\mathbf{R}_p} V_{\mathrm{es}}(\mathbf{r})$. Hence, by Eq. (19), the phonon perturbation in the Wannier representation will exhibit a spatial localization similar to the interatomic force constants.

The spatial decay of the force constants has been thoroughly discussed elsewhere,[32,58] and we summarize here only the aspects which are relevant to the present work. In metals, the electrostatic interactions are efficiently screened within a few bond lengths; therefore, the force constants are short ranged. In some cases, the topology of the Fermi surface gives rise to Kohn anomalies, which correspond to long-ranged force constants propagating along the wave vector associated with the anomaly. In such cases, the spatial decay of $C(\boldsymbol{\tau}_{\kappa p}, \boldsymbol{\tau}_{\kappa' p'})$ will depend on the strength of the anomaly and must be analyzed carefully before proceeding with the methods described in Sec. IV. The possibility of long-ranged interatomic force constants related to Friedel oscillations has also been pointed out in Ref. 58. However, to the authors' knowledge, no first-principles investigations report long-ranged force constants associated with this effect. In polar insulators, the Born dynamical charges are nonvanishing, and the force constants are long ranged due to their dipolar interactions.[59] In such cases, the procedure described in this work can still be applied by separating the short-range analytical part of the dynamical matrix from the long-range nonanalytic term.[58]

### C. Electron-phonon matrix element

In order to obtain the e-ph vertex in the joint electron-phonon Wannier representation, we combine Eqs. (6), (10), and (17). After rearranging the terms, we find

$$\begin{aligned}\langle m\mathbf{k}+\mathbf{q}|\partial_{\mathbf{q}\nu}V|n\mathbf{k}\rangle &= \frac{1}{N_e^2}\sum_{m'n'\kappa}\sum_{\mathbf{R}_e\mathbf{R}'_e\mathbf{R}_p} e^{i[\mathbf{k}\cdot(\mathbf{R}_e-\mathbf{R}'_e)+\mathbf{q}\cdot(\mathbf{R}_p-\mathbf{R}'_e)]}\mathbf{u}^{\nu}_{\mathbf{q}\kappa} \\ &\quad\cdot U_{mm',\mathbf{k}+\mathbf{q}}\langle m'\mathbf{R}'_e|\partial_{\kappa,\mathbf{R}_p}V|n'\mathbf{R}_e\rangle U^{\dagger}_{n'n,\mathbf{k}}.\end{aligned} \tag{20}$$

Now, we exploit the translational invariance of the "three-point" matrix element:

$$\langle m'\mathbf{R}'_e|\partial_{\kappa,\mathbf{R}_p}V|n'\mathbf{R}_e\rangle = \langle m'0_e|\partial_{\kappa,\mathbf{R}_p-\mathbf{R}'_e}V|n'\mathbf{R}_e-\mathbf{R}'_e\rangle, \tag{21}$$

which is obtained by writing the integral over the infinite crystal and performing a change of variables. In Eq. (21), $|m'\mathbf{0}_e\rangle$ is a Wannier function centered in the unit cell at the origin of the reference frame. By substituting Eq. (21) into Eq. (20) and changing the variables $\mathbf{R}_e-\mathbf{R}'_e$ into $\mathbf{R}_e$ and $\mathbf{R}_p-\mathbf{R}'_e$ into $\mathbf{R}_p$ we find

$$g(\mathbf{k},\mathbf{q}) = \frac{1}{N_{\mathbf{e}}}\sum_{\mathbf{R}_e,\mathbf{R}_p} e^{i(\mathbf{k}\cdot\mathbf{R}_e+\mathbf{q}\cdot\mathbf{R}_p)} U_{\mathbf{k}+\mathbf{q}}\, g(\mathbf{R}_e,\mathbf{R}_p)\, U^{\dagger}_{\mathbf{k}}\mathbf{u}_{\mathbf{q}}, \tag{22}$$

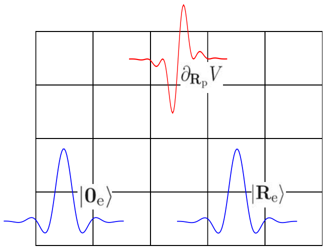

FIG. 2. (Color online) Simplified scheme of the electron and phonon Wannier functions entering the three-point e-ph matrix element [Eq. (23)]. The square lattice indicates the unit cells of the crystal, the red lines the electron Wannier functions $|\mathbf{0}_e\rangle$ and $|\mathbf{R}_e\rangle$, and the blue line the phonon perturbation in the Wannier representation $\partial_{\mathbf{R}_p}V$. Whenever two of these functions are centered on distant unit cells, the e-ph matrix element in the Wannier representation $\langle\mathbf{0}_e|\partial_{\mathbf{R}_p}V|\mathbf{R}_e\rangle$ vanishes.

having introduced the e-ph vertex in the Wannier representation:

$$g_{mn,\nu}(\mathbf{R}_e,\mathbf{R}_p) = \langle m\mathbf{0}_e|\partial_{\nu,\mathbf{R}_p}V|n\mathbf{R}_e\rangle. \tag{23}$$

In Eq. (22), we omitted band and branch indices for clarity, keeping in mind that the electronic matrices $U_{\mathbf{k}}$ and $U_{\mathbf{k}+\mathbf{q}}$ act on the band indices of $g(\mathbf{R}_e,\mathbf{R}_p)$ and the phonon matrix $\mathbf{u}_{\mathbf{q}}$ acts on the corresponding branch index. We notice that the "band" and "branch" indices do not have any special meaning in the Wannier representation: In the electron case, they label different Wannier functions belonging to the same unit cell, and in the phonon case, they label a particular atom in the unit cell as well as the Cartesian direction of the corresponding displacement. In order to express the e-ph matrix element in the Wannier representation in terms of the corresponding Bloch vertex, we invert Eq. (23):

$$g(\mathbf{R}_e,\mathbf{R}_p) = \frac{1}{N_p}\sum_{\mathbf{k},\mathbf{q}} e^{-i(\mathbf{k}\cdot\mathbf{R}_e+\mathbf{q}\cdot\mathbf{R}_p)} U^{\dagger}_{\mathbf{k}+\mathbf{q}}\, g(\mathbf{k},\mathbf{q})\, U_{\mathbf{k}}\mathbf{u}^{-1}_{\mathbf{q}}. \tag{24}$$

The striking feature of the Wannier vertex [Eq. (24)] is the localization in both the electron and phonon variables. As illustrated in Fig. 2, $\langle m\mathbf{0}_e|\partial_{\nu,\mathbf{R}_p}V|n\mathbf{R}_e\rangle$ vanishes whenever $\mathbf{R}_e$ or $\mathbf{R}_p$ corresponds to a unit cell sufficiently distant from the origin of the reference frame. As a consequence, in order to accurately describe the e-ph interaction in a given system, we only need to know a small number of matrix elements in the Wannier representation. This elementary observation constitutes the core of this study.

The relevant range of $\mathbf{R}_e$ and $\mathbf{R}_p$ in Eq. (22) depends on the localization of the electronic Wannier functions and of the phonon perturbations in the Wannier representation. Inspection of Eq. (23) indicates that the spatial decay of the matrix elements is bound by the limiting cases $g_{mn,\nu}(\mathbf{R}_e,\mathbf{0}_p)$ and $g_{mn,\nu}(\mathbf{0}_e,\mathbf{R}_p)$. In the first case, the vertex corresponds to the overlap between $w^{\star}_m(\mathbf{r})\nabla_{\tau_\kappa}V(\mathbf{r})$ and $w_n(\mathbf{r}-\mathbf{R}_e)$. When the phonon perturbation is sufficiently localized, the matrix element is found to scale as $g_{mn,\nu}(\mathbf{R}_e,\mathbf{0}_p)\sim w_n(\mathbf{R}_e)$. Therefore, in this case, the spatial decay is dictated by the localization of the electronic Wannier functions. In the second case, the matrix element corresponds to the overlap between $w_m^\star(\mathbf{r})w_n(\mathbf{r})$ and the phonon perturbation $\nabla_{\tau_\kappa}V(\mathbf{r}-\mathbf{R}_p)$ (assuming for simplicity local pseudopotentials). For sufficiently localized electronic Wannier functions, the matrix element is found to scale as $g_{mn,\nu}(\mathbf{0}_e,\mathbf{R}_p)\sim\nabla V(\mathbf{R}_p)$, indicating that the spatial decay of the e-ph vertex is determined in this case by the localization of the phonon perturbation. More generally, the slowest decay among these two limiting cases sets the size of the real-space supercell or the **k**-point sampling to be considered.

Equations (22) and (24) provide a compact and elegant transformation between the e-ph matrix element in the Bloch and the Wannier representations. Interestingly, Eq. (22) is reminiscent of the expressions used in tight-binding calculations to model the e-ph interaction.[60] We notice, however, that our expressions [Eqs. (22) and (24)] provide a fully *first-principles* description of the e-ph interaction. This observation suggests a systematic approach to determine tight-binding parameters for the e-ph interaction by first performing *ab initio* calculations in the Bloch representation and then determining the e-ph vertex in the Wannier representation through Eq. (24). An accurate tight-binding parametrization of the e-ph interaction would prove useful in the study of large-scale systems or systems with disorder.[35]

## IV. WANNIER-FOURIER INTERPOLATION

In this section, we describe how to exploit the spatial localization in the Wannier representation to calculate the quantities required in the self-energies [Eqs. (3) and (4)] by a generalized Wannier-Fourier interpolation. We first discuss the transformation of the electron eigenstates and eigenvalues, the vibrational modes and frequencies, as well as the e-ph matrix elements from a coarse Brillouin-zone grid $(\mathbf{k},\mathbf{q})$ to the Wannier representation $(\mathbf{R}_e,\mathbf{R}_p)$ in the corresponding real-space supercell. Then, we describe the reverse process from the Wannier representation to the Bloch representation at a new set of electron and phonon momenta $(\mathbf{k}',\mathbf{q}')$.

### A. Bloch to Wannier transform

#### 1. Electrons

We calculate the one-particle electronic eigenstates $\psi_{n\mathbf{k}}(\mathbf{r})$ and eigenvalues $\epsilon_{n\mathbf{k}}$ by adopting standard density-functional techniques.[61–63] The matrix elements of the single-particle Kohn-Sham Hamiltonian $\hat{H}^{\mathrm{el}}$ in the Bloch representation are

$$H^{\mathrm{el}}_{mn,\mathbf{k}}=\langle m\mathbf{k}|\hat{H}^{\mathrm{el}}|n\mathbf{k}\rangle=\delta_{mn}\epsilon_{n\mathbf{k}}. \tag{25}$$

In Eq. (25), the **k** vectors correspond to a uniform grid of size $N_1^e\times N_2^e\times N_3^e$ centered at the $\Gamma$ point (we assume a three-dimensional system here; the extension to systems with reduced dimensionality is obvious). The uniform and unshifted grid is required to perform the Fourier transform [Eq. (9)]. The eigenstates $|n\mathbf{k}\rangle$ and eigenvalues $\epsilon_{n\mathbf{k}}$ are used to determine the unitary matrix $U_\mathbf{k}$ for the transformation to maximally localized Wannier functions. This step involves the calculation of the matrix elements of the periodic position operator[49] and is performed using the method of Refs. 49 and 64.

Once the unitary matrix $U_\mathbf{k}$ has been determined, we calculate the electronic Hamiltonian in the Wannier representation by combining Eqs. (9) and (25):

$$H^{\mathrm{el}}_{\mathbf{R}_e,\mathbf{R}'_e}=\langle\mathbf{R}_e|\hat{H}^{\mathrm{el}}|\mathbf{R}'_e\rangle=\sum_{\mathbf{k}}e^{-i\mathbf{k}\cdot(\mathbf{R}'_e-\mathbf{R}_e)}U^\dagger_\mathbf{k}H^{\mathrm{el}}_\mathbf{k}U_\mathbf{k}, \tag{26}$$

where band indices are omitted for clarity. By construction, the Hamiltonian in the Wannier representation $H^{\mathrm{el}}_{\mathbf{R}_e,\mathbf{R}'_e}$ decays with the distance $|\mathbf{R}_e-\mathbf{R}'_e|$. The length scale for the spatial decay is determined by the localization of the electronic Wannier functions.

#### 2. Phonons

We calculate vibrational eigenmodes $\mathbf{e}^\nu_\kappa(\mathbf{q})$ and eigenfrequencies $\omega_{\mathbf{q}\nu}$ through density-functional perturbation theory.[32] This operation is performed for all the **q** vectors belonging to a uniform grid of size $N_1^p\times N_2^p\times N_3^p$ centered at the $\Gamma$ point (in Sec. V D, we describe how to restrict the **q** points to the irreducible wedge of the Brillouin zone). The use of a uniform and unshifted grid is needed for the Fourier transform in Eq. (18), similarly to the electronic case (cf. Sec. IV A 1). The dynamical matrix in the Bloch representation for phonons is, by definition,

$$D^{\mathrm{ph}}_{\mathbf{q},\mu\nu}=\langle\mathbf{q}\mu|\hat{D}^{\mathrm{ph}}|\mathbf{q}\nu\rangle=\delta_{\mu\nu}\omega^2_{\mathbf{q}\nu}. \tag{27}$$

Using Eq. (27) and the completeness relation $\Sigma_{\kappa p}|\boldsymbol{\tau}_{\kappa p}\rangle\langle\boldsymbol{\tau}_{\kappa p}|=1$, we obtain the dynamical matrix in the phonon Wannier representation:

$$\langle\boldsymbol{\tau}_{\kappa'p'}|\hat{D}^{\mathrm{ph}}|\boldsymbol{\tau}_{\kappa p}\rangle=\sum_{\mathbf{q},\mu\nu}e^{-i\mathbf{q}\cdot(\mathbf{R}'_p-\mathbf{R}_p)}\mathbf{e}_{\mathbf{q}\kappa'}D^{\mathrm{ph}}_{\mathbf{q},\mu\nu}\mathbf{e}^\dagger_{\mathbf{q}\kappa}. \tag{28}$$

If we collect the atom label $\kappa$ and the Cartesian direction $\alpha$ of $\tau_{\kappa\alpha}$ into a composite index $\nu=\kappa\alpha$, the vibrational eigenmodes can be expressed in terms of the square matrices $(e_\mathbf{q})_{\mu\nu}$. Accordingly, Eq. (28) can be rewritten in a compact fashion which highlights the analogy with Eq. (26):

$$D^{\mathrm{ph}}_{\mathbf{R}_p,\mathbf{R}'_p}=\langle\mathbf{R}_p|\hat{D}^{\mathrm{ph}}|\mathbf{R}'_p\rangle=\sum_{\mathbf{q}}e^{-i\mathbf{q}\cdot(\mathbf{R}'_p-\mathbf{R}_p)}e_\mathbf{q}D^{\mathrm{ph}}_\mathbf{q}e^\dagger_\mathbf{q}. \tag{29}$$

In order to make connection with the standard terminology, we observe that the left-hand side of Eq. (28) is related to the matrix of the interatomic force constants by[58]

$$\langle\boldsymbol{\tau}_{\kappa'p'}|\hat{D}^{\mathrm{ph}}|\boldsymbol{\tau}_{\kappa p}\rangle=(m_\kappa m_{\kappa'})^{-1/2}C(\boldsymbol{\tau}_{\kappa p},\boldsymbol{\tau}_{\kappa'p'}). \tag{30}$$

So far, the formalism for the lattice dynamics has been described in complete analogy with the electronic case. There is, however, an important difference between these cases when it comes to the spatial decay of the operators $\hat{H}^{\mathrm{el}}$ and $\hat{D}^{\mathrm{ph}}$. On the one hand, the Kohn-Sham one-particle Hamiltonian is *local* in real space (the nonlocality eventually arising from the pseudopotentials being short ranged); therefore, the spatial decay of $H^{\text{el}}_{\mathbf{R}_e,\mathbf{R}'_e}$ is dictated by the overlap of the Wannier functions at $\mathbf{R}_e$ and $\mathbf{R}'_e$. On the other hand, while the phonon Wannier functions are always infinitely localized by construction (cf. Sec. III B), the operator $\hat{D}^{\text{ph}}$ is *nonlocal* in real space, as it is clear from Eq. (30). As a consequence, the localization of $D^{\text{ph}}_{\mathbf{R}_p,\mathbf{R}'_p}$ does not relate to the overlap of lattice Wannier functions, but instead to the effectiveness of the dielectric screening in the material, as discussed in relation to Eq. (19).

### *3. Electron-phonon matrix elements*

The e-ph matrix elements are computed after the electronic eigenstates and eigenvalues and the phonon eigenmodes and eigenfrequencies have been determined. We calculate the matrix elements $g_{mn,\nu}(\mathbf{k},\mathbf{q})$ in the Bloch representation [Eq. (6)] using the variation of the self-consistent potential $\partial_{\mathbf{q}\nu}V$ determined by density-functional perturbation theory.[32] The $\mathbf{k}$ and $\mathbf{q}$ points belong to the uniform unshifted Brillouin-zone grids with $N_1^e \times N_2^e \times N_3^e$ and $N_1^p \times N_2^p \times N_3^p$ points, respectively.

The computation of the dynamical matrix is the most expensive step in the procedure; therefore, it is convenient to restrict the set of $\mathbf{q}$ points to the irreducible wedge of the Brillouin zone. The remaining points and the associated eigenmodes, eigenfrequencies, and perturbations can be generated by exploiting the crystal symmetries (cf. Sec. V D). The electronic eigenstates are computed on the full uniform grid, i.e., no symmetry reduction is applied in the electronic case. This choice is motivated by the observation that even if the $\mathbf{k}$ vector in the e-ph matrix elements is restricted to the irreducible wedge, the $\mathbf{k}+\mathbf{q}$ vector spans the whole Brillouin zone since $\mathbf{q}$ belongs to a uniform grid.

Once the e-ph matrix elements are calculated in the Bloch representation, we use Eq. (24) to transform them into the Wannier representation. The required transformation matrices $U_{\mathbf{k}}$ and $\mathbf{u}_{\mathbf{q}}$ are already available from the previous steps [Secs. IV A 1 and IV A 2]. Whenever the $\mathbf{k}$ and $\mathbf{q}$ grids are *commensurate*, the electronic transformation matrices $U_{\mathbf{k}+\mathbf{q}}$ are conveniently obtained by mapping the $\mathbf{k}+\mathbf{q}$ points into the original grid of points $\mathbf{k}$. When $\mathbf{k}+\mathbf{q}$ falls outside the uniform $N_1^e \times N_2^e \times N_3^e$ grid, we use parallel transport and set $U_{\mathbf{k}+\mathbf{q}} = U_{\mathbf{k}+\mathbf{q}+\mathbf{G}}$, where $\mathbf{G}$ is the reciprocal lattice vector which folds $\mathbf{k}+\mathbf{q}$ back in the original $\mathbf{k}$ grid. It is worth stressing that this procedure requires only *one single minimization* of the spread functional to determine maximally localized Wannier functions. The choice of commensurate $\mathbf{k}$ and $\mathbf{q}$ grids does not represent a limitation, since the two grids are already assumed to be uniform and unshifted. One possible exception is discussed in Sec. V A.

## B. Wannier to Bloch transform

### *1. Electrons*

We wish to calculate electronic eigenstates $|n\mathbf{k}'\rangle$ and eigenvalues $\epsilon_{n\mathbf{k}'}$ for a set of wave vectors $\mathbf{k}'$ on a significantly finer grid than the original one with $N_1^e \times N_2^e \times N_3^e$ points. According to the application at hand, we could adopt a uniform grid, a grid extending over the irreducible wedge of the Brillouin zone, or a path along relevant high-symmetry lines. In the transformation from the Wannier to the Bloch representation, a uniform and unshifted grid is no longer required (cf. Sec. IV A 1).

By combining Eqs. (10), (25), and (26), we obtain

$$H^{\text{el}}_{\mathbf{k}'} = U_{\mathbf{k}'}\left(\frac{1}{N_e}\sum_{\mathbf{R}_e} e^{i\mathbf{k}'\cdot\mathbf{R}_e} H^{\text{el}}_{\mathbf{0}_e,\mathbf{R}_e}\right) U^{\dagger}_{\mathbf{k}'}, \tag{31}$$

where we have omitted band indices for clarity. In Eq. (31), the sum extends over the unit cells $\mathbf{R}_e$ belonging to the Wigner-Seitz supercell corresponding to $N_1^e \times N_2^e \times N_3^e$ replicas of the primitive cell. For $\mathbf{R}_e$ outside this Wigner-Seitz volume, we *assume* that the matrix elements of the Hamiltonian $H^{\text{el}}_{\mathbf{0}_e,\mathbf{R}_e}$ are negligibly small. The quality of the final results strictly relies on this assumption, which must be verified numerically before proceeding with the calculations.

In Eq. (31), the only known quantity is contained within the brackets. We do not know at this stage the transformation matrices $U_{\mathbf{k}'}$ for the new points $\mathbf{k}'$, nor we can determine maximally localized Wannier functions through the method of Ref. 49 since the Bloch eigenvalues and eigenstates at $\mathbf{k}'$ are unknown as well. However, we do know that, by construction, the Hamiltonian $H_{\mathbf{k}'}$ on the left-hand side of Eq. (31) is diagonal in the band indices [cf. Eq. (25)]. This implies that the $U_{\mathbf{k}'}$ matrix is nothing but the diagonalizer of the term within the brackets $N_e^{-1}\Sigma_{\mathbf{R}_e}\exp(i\mathbf{k}'\cdot\mathbf{R}_e)H^{\text{el}}_{\mathbf{0}_e,\mathbf{R}_e}$. Therefore, to find eigenstates and eigenvalues of the electronic Hamiltonian at an arbitrary wave vector $\mathbf{k}'$, we need to perform (i) a Fourier interpolation of the Hamiltonian in the Wannier representation, corresponding to the term within the brackets in Eq. (31), and (ii) a diagonalization of the resulting matrix, yielding $U_{\mathbf{k}'}$, $\epsilon_{n\mathbf{k}'}$, as well as the new Bloch eigenstates $|n\mathbf{k}'\rangle$ through Eq. (9). The procedure outlined in this section was first proposed in Ref. 53 and subsequently applied to the study of the anomalous Hall effect[65] and the magnetic circular dichroism.[66]

### *2. Phonons*

The calculation of phonon eigenmodes and eigenfrequencies at a new set of $\mathbf{q}'$ points proceeds along the same lines as for the electrons (Sec. IV B 1). The new set of points $\mathbf{q}'$ may correspond to a fine mesh (not necessarily uniform) or to a path in reciprocal space, depending on the application. We formally invert Eq. (29) to obtain

$$D^{\text{ph}}_{\mathbf{q}'} = e^{\dagger}_{\mathbf{q}'}\left(\frac{1}{N_p}\sum_{\mathbf{R}_p} e^{i\mathbf{q}'\cdot\mathbf{R}_p} D^{\text{ph}}_{\mathbf{0}_p,\mathbf{R}_p}\right) e_{\mathbf{q}'}, \tag{32}$$

in complete analogy with the corresponding expression for the electrons [Eq. (31)]. In Eq. (32), the sum extends over the unit cells $\mathbf{R}_p$ belonging to the Wigner-Seitz cell constructed for the supercell with $N_1^p \times N_2^p \times N_3^p$ replicas of the primitive cell. The matrix elements of the dynamical matrix in the Wannier representation $D^{\text{ph}}_{\mathbf{0}_p,\mathbf{R}_p}$ are *assumed* to be vanishing outside this Wigner-Seitz supercell. In practice, the length scale of the spatial decay of $D^{\text{ph}}_{\mathbf{0}_p,\mathbf{R}_p}$ with $\mathbf{R}_p$ determines the

TABLE I. Summary of the Wannier-Fourier interpolation scheme from a set of matrix elements on a uniform grid $(\mathbf{k},\mathbf{q})$ to another set with arbitrary momenta $(\mathbf{k}',\mathbf{q}')$. The leftmost column contains input quantities determined by density-functional calculations. The second column indicates the operations required to transform from the Bloch to the Wannier representation. The quantities in the Wannier representation thus obtained are reported in the third column. At this stage, we could work directly within the Wannier representation, or transform back to the Bloch representation by Fourier interpolation. The inverse transforms are indicated in the fourth column, while the rightmost column gives the final quantities.

| | Bloch | Bloch → Wannier | Wannier | Wannier → Bloch | Bloch |
|---|---|---|---|---|---|
| Electrons | $H_{\mathbf{k}}^{\mathrm{el}}$<br>$U_{\mathbf{k}}$ | Rotate $H_{\mathbf{k}}^{\mathrm{el}}$ with $U_{\mathbf{k}}$ and Fourier transform [Eq. (26)] | $H_{\mathbf{R}_e,\mathbf{R}_e'}^{\mathrm{el}}$ | Inverse Fourier transform $H_{\mathbf{R}_e,\mathbf{R}_e'}^{\mathrm{el}}$ to $\mathbf{k}'$ and diagonalize [Eq. (31)] | $H_{\mathbf{k}'}^{\mathrm{el}}$<br>$U_{\mathbf{k}'}$ |
| Phonons | $D_{\mathbf{q}}^{\mathrm{ph}}$<br>$e_{\mathbf{q}}$ | Rotate $D_{\mathbf{q}}^{\mathrm{ph}}$ with $e_{\mathbf{q}}$ and Fourier transform [Eq. (29)] | $D_{\mathbf{R}_p,\mathbf{R}_p'}^{\mathrm{ph}}$ | Inverse Fourier transform $D_{\mathbf{R}_p,\mathbf{R}_p'}^{\mathrm{ph}}$ to $\mathbf{q}'$ and diagonalize [Eq. (32)] | $D_{\mathbf{q}'}^{\mathrm{ph}}$<br>$e_{\mathbf{q}'}$ |
| e-ph matrix elements | $g(\mathbf{k},\mathbf{q})$<br>$U_{\mathbf{k}}$, $U_{\mathbf{k+q}}$, $\mathbf{e}_{\mathbf{q}}$ | Rotate $g(\mathbf{k},\mathbf{q})$ with $U_{\mathbf{k}}$, $U_{\mathbf{k+q}}$, $e_{\mathbf{q}}$, and Fourier transform [Eq. (24)] | $g(\mathbf{R}_e,\mathbf{R}_p)$ | Inverse Fourier transform $g(\mathbf{R}_e,\mathbf{R}_p)$ to $\mathbf{k}'$, $\mathbf{q}'$ and rotate with $U_{\mathbf{k}'}$, $U_{\mathbf{k}'+\mathbf{q}'}$, and $e_{\mathbf{q}'}$ [Eq. (22)] | $g(\mathbf{k}',\mathbf{q}')$ |

size of the original mesh of points $N_1^p \times N_2^p \times N_3^p$ required for a given target accuracy.

As for the electrons (cf. Sec. IV B 1), the known quantity in Eq. (31) is the term within the brackets, and the matrix on the left-hand side is diagonal by construction [cf. Eq. (27)]. Hence, the eigenmodes $\mathbf{e}_{\mathbf{q}'}$ at the new $\mathbf{q}'$ points must be found by diagonalizing the term within the brackets $N_p^{-1}\Sigma_{\mathbf{R}_p} \exp(i\mathbf{q}'\cdot\mathbf{R}_p) D^{\mathrm{ph}}_{\mathbf{0}_p,\mathbf{R}_p}$. Even in the case of phonons, the determination of eigenfrequencies and eigenmodes at arbitrary momenta $\mathbf{q}'$ requires two steps: (i) a Fourier interpolation of the dynamical matrix in the Wannier representation, corresponding to the term within brackets in Eq. (32), and (ii) a diagonalization of the resulting matrix, yielding the eigenmodes $\mathbf{e}_{\mathbf{q}'}$ and squared eigenfrequencies $\omega^2_{\mathbf{q}'\nu}$. This procedure corresponds to the standard approach used to compute complete phonon dispersions starting from a small grid in the Brillouin zone.[32,58]

#### 3. Electron-phonon matrix elements

The calculation of the e-ph matrix element in the new sets of points $\mathbf{k}'$ and $\mathbf{q}'$ is performed by using Eqs. (22) and the transformation matrices $U_{\mathbf{k}'}$, $U_{\mathbf{k}'+\mathbf{q}'}$, and $\mathbf{e}_{\mathbf{q}'}$ determined in the previous steps [Secs. IV B 1 and IV B 2]. After this operation, we have all the ingredients needed to evaluate the physical quantities in Eqs. (3), (4), (7), and (8), with an accurate and ultradense sampling of the Brillouin zone. The entire Wannier-Fourier interpolation procedure described in this section is summarized in Table I.

## V. SPECIAL CASES AND PRACTICAL DETAILS

### A. Electron-only Wannier representation

In some applications, we could be interested in the self-energy of only a limited set of phonon modes (for instance, modes at high-symmetry points), rather than the whole vibrational spectrum in the Brillouin zone. In such cases, calculating the dynamical matrix for every $\mathbf{q}$ vector in a uniform grid as described in Sec. IV A 2 may turn out to be too expensive from a computational standpoint, and it is desirable to find an alternative path.

The easiest way to proceed in such cases consists in transforming the electronic states in the Wannier representation (Sec. III A) while keeping the phonon perturbation (Sec. III B) in the Bloch representation. The transformation laws of the e-ph vertex in such electron-only Wannier representation read

$$g(\mathbf{k},\mathbf{q}) = \frac{1}{N_e}\sum_{\mathbf{R}_e} e^{i\mathbf{k}\cdot\mathbf{R}_e} U_{\mathbf{k+q}}\, g(\mathbf{R}_e,\mathbf{q})\, U_{\mathbf{k}}^{\dagger}, \tag{33}$$

$$g(\mathbf{R}_e,\mathbf{q}) = \sum_{\mathbf{k}} e^{-i\mathbf{k}\cdot\mathbf{R}_e} U_{\mathbf{k+q}}^{\dagger}\, g(\mathbf{k},\mathbf{q})\, U_{\mathbf{k}}, \tag{34}$$

with the e-ph matrix element in the mixed representation given by

$$g_{mn,\nu}(\mathbf{R}_e,\mathbf{q}) = \langle m\mathbf{0}_e|\partial V_{\mathbf{q}\nu}|n\mathbf{R}_e\rangle . \tag{35}$$

In this case, the wave vector $\mathbf{q}$ is not required to be commensurate with the uniform electronic grid. Accordingly, two minimizations (for every wave vector $\mathbf{q}$) of the Berry-phase spread functional are required to determine maximally localized Wannier functions: one for the set of states $\{\psi_{n\mathbf{k}}\}$, yielding the matrix $U_{\mathbf{k}}$, and another one for the set $\{\psi_{n\mathbf{k+q}}\}$, providing the matrix $U_{\mathbf{k+q}}$. The inverse transformation from the Wannier to the Bloch representation on arbitrary points $\mathbf{k}'$ proceeds as described in Sec. IV B 1.

### B. Zone-center phonons and frozen-phonon methods

In the case of a very large system in a supercell geometry, it could be convenient to restrict the sampling of the vibrational Brillouin zone to the $\Gamma$ point only. This is appropriate whenever the interatomic force constants decay to negligible values over a distance smaller than the size of the supercell. This situation corresponds to the case $\mathbf{q}=\mathbf{0}$ of the electron-only interpolation described in Sec. V A and only requires the determination of the transformation matrices $U_{\mathbf{k}}$ once.

This situation is also interesting because the procedure described so far can be performed without resorting to linear-response techniques: the matrix of the interatomic force constants [Eq. (30)] can be calculated by taking finite differences of the total energy (frozen-phonon approach),[67] and our procedure can be implemented as a postprocessing step in any electronic-structure package performing total-energy calculations.

### C. Gauge arbitrariness

The diagonalization of the Kohn-Sham single-particle Hamiltonian determines the eigenfunctions $\psi_{n\mathbf{k}}$ up to an arbitrary phase factor. In the presence of accidental degeneracies, the arbitrariness also includes a unitary transformation within the degenerate manifold. In general, this gauge arbitrariness bears no implications on the calculation of ground-state properties such as total energies and its derivatives. However, the actual localization of the Wannier functions [Eq. (9)] crucially depends on the phases of the wave functions and may be compromised if this gauge freedom is not dealt with properly. Indeed, small variations in the procedures adopted to diagonalize the Hamiltonian may lead to completely different phase settings. This is especially important since the calculation of maximally localized Wannier functions and the calculation of the e-ph matrix elements are performed as two separate and subsequent steps.

Different phase settings may arise, for instance, (i) when the eigenstates used to determine $U_{\mathbf{k}}$ with the procedure of Ref. 49 are obtained with a different diagonalization algorithm than that used in the calculation of the e-ph matrix elements; (ii) when different algorithms are used to deal with the cases $\mathbf{q}=\mathbf{0}$ or $\mathbf{q}\neq\mathbf{0}$; (iii) when $\mathbf{k}+\mathbf{q}$ falls outside the first Brillouin zone and can be folded into another point $\mathbf{k}^\star$ in the first zone, but the Bloch phases $\exp[i(\mathbf{k}+\mathbf{q})\cdot\mathbf{r}]$ and $\exp(i\mathbf{k}^\star\cdot\mathbf{r})$ modify the Fourier coefficients of the nonlocal projectors of the pseudopotentials; and (iv) when different architectures or different parallel environments within the same architecture are used for the calculation of $U_{\mathbf{k}}$ and the e-ph matrix elements $g_{mn,\nu}(\mathbf{k},\mathbf{q})$, respectively.

It is therefore desirable to fix a unique and unambiguous gauge for the wave functions. We can accomplish this in two separate steps: we first set the gauge within each degenerate manifold, and then we set the phase of every eigenstate individually. The latter step is straightforwardly performed by requiring the wave functions $\psi_{n\mathbf{k}}(\mathbf{r})$ to be real valued at some arbitrarily chosen point $\mathbf{r}$. In a plane-wave formalism, the same goal can be achieved more efficiently by requiring the largest Fourier component of the wave functions to be real valued. In practice, it is sufficient to search for the largest coefficient in a small subset of plane waves. The first step is performed by borrowing standard techniques from degenerate perturbation theory.[68] To this end, we consider a fictitious perturbation $\alpha\hat{V}^{\mathrm{fict}}$ which lifts the degeneracies of the Hamiltonian. We compute the matrix elements of this perturbation in the degenerate manifold:

$$V^{\mathrm{fict}}_{mn}=\langle m\mathbf{k}|\hat{V}^{\mathrm{fict}}|n\mathbf{k}\rangle, \tag{36}$$

and we diagonalize the perturbation to find the new eigenstates:

$$[B^\dagger_{\mathbf{k}}V^{\mathrm{fict}}B_{\mathbf{k}}]_{mn}=\delta_{mn}v^{\mathrm{fict}}_n, \tag{37}$$

with $v^{\mathrm{fict}}_n$ being the eigenvalues of the fictitious perturbation. At this point, we consider the new eigenstates

$$\psi'_{n\mathbf{k}}=\sum_m B_{\mathbf{k},nm}\psi_{m\mathbf{k}}, \tag{38}$$

which diagonalize the Hamiltonian $\hat{H}^{\mathrm{el}}+\alpha\hat{V}^{\mathrm{fict}}$ and are nondegenerate by construction. The strength $\alpha$ of the fictitious perturbation is now set to zero to recover the eigenvalues of the original Hamiltonian. In order for the gauge matrix $B_{\mathbf{k}}$ to be unitary, the perturbation $\hat{V}^{\mathrm{fict}}$ must be chosen Hermitian. This is achieved by constructing a real-valued local fictitious potential which does not contain any of the symmetries of the Hamiltonian.

It is worth noting at this point that the e-ph matrix element $g_{mn,\nu}(\mathbf{k},\mathbf{q})$ is not a gauge-invariant quantity itself, since both the electronic eigenstates and the phonon eigenmodes are defined up to a phase (possibly a unitary matrix). This is consistent with the fact that the matrix element is not a physical observable. On the other hand, the self-energies [Eqs. (3) and (4)] contribute to the electron and phonon spectral functions, which are physical observables (for instance, by photoemission or tunneling experiments). Therefore, we expect the self-energies $\Sigma_{\mathbf{k}}(\omega)$ and $\Pi_{\mathbf{q}}(\omega)$ to be gauge invariant. This is actually the case, because the quantities $\Sigma_{m\nu}|g_{mn,\nu}(\mathbf{k},\mathbf{q})|^2$ and $\Sigma_{mn}|g_{mn,\nu}(\mathbf{k},\mathbf{q})|^2$ entering Eqs. (3) and (4) are both gauge invariant when the summations are restricted to degenerate subspaces (this property corresponds to the invariance of the Fröbenius norm under similarity transforms).

### D. Irreducible wedge of the Brillouin zone

The most computationally intensive part of the procedure described thus far is represented by the calculation of the vibrational eigenmodes, eigenfrequencies, and the associated phonon perturbation for all the $\mathbf{q}$ points needed in the Fourier transforms [Eqs. (17) and (24)]. It is therefore important to consider the possibility of restricting the set of the required $\mathbf{q}$ vectors to the irreducible wedge of the Brillouin zone.

The irreducible $\mathbf{q}$ points are determined by considering the set of vectors which are nonequivalent under the symmetry operations of the crystal point group. We follow the convention of Ref. 69 in labeling the symmetry operations as $\{\mathcal{S}|\mathbf{v}\}$, in such a way that $\{\mathcal{S}|\mathbf{v}\}\mathbf{r}=\mathcal{S}\mathbf{r}+\mathbf{v}$, with $\mathcal{S}$ being the rotational part (proper or improper) of the symmetry operation and $\mathbf{v}$ the eventually associated fractional translation. Given a $\mathbf{q}$ vector in the irreducible part of the Brillouin zone, we can generate the so-called star of $\mathbf{q}$ by applying all the crystal symmetry operations.

Once the dynamical matrix and the phonon perturbation for an irreducible $\mathbf{q}$ point have been calculated, the corresponding quantities for a wave vector $\mathcal{S}\mathbf{q}$ belonging to the star of $\mathbf{q}$ can be determined by exploiting the transformation properties of the vibrational eigenmodes under the symmetry operation $\{\mathcal{S}|\mathbf{v}\}$. The transformation law for the eigenmodes is given by[69]

$$\mathbf{e}_{\mathcal{S}\mathbf{q}}=\Gamma_{\{\mathcal{S}|\mathbf{v}\}}(\mathbf{q})\mathbf{e}_{\mathbf{q}}, \tag{39}$$

where the unitary matrix $\Gamma_{\{\mathcal{S}|\mathbf{v}\}}(\mathbf{q})$ is defined as

$$[\Gamma_{\{\mathcal{S}|\mathbf{v}\}}(\mathbf{q})]_{\alpha\beta}^{\kappa\kappa'} = \mathcal{S}_{\alpha\beta}\delta_{\kappa,F_{\mathcal{S}}(\kappa')}e^{i\mathcal{S}\mathbf{q}\cdot[\boldsymbol{\tau}_\kappa-\{\mathcal{S}|\mathbf{v}\}\boldsymbol{\tau}_{\kappa'}]}. \tag{40}$$

In Eq. (40) $\alpha$ and $\beta$ indicate Cartesian directions, and $F_{\mathcal{S}}(\kappa')$ represents the atom that $\kappa'$ is brought into by the symmetry operation $\{\mathcal{S}|\mathbf{v}\}$. Equation (39) implicitly assumes that eigenmodes at $\mathbf{q}$ and $\mathcal{S}\mathbf{q}$ carry no phase difference and that no gauge mixing occurs whenever two or more eigenmodes are degenerate. This choice implies that, when transforming the dynamical matrix and the e-ph matrix elements from the Bloch to the Wannier representation, one cannot directly apply the symmetry $\{\mathcal{S}|\mathbf{v}\}$ to the interatomic force constants and then diagonalize the resulting dynamical matrix.[32] Indeed, such procedure would lead to eigenmodes which do not obey the phase relations defined by Eq. (39). The correct procedure instead is to first transform the eigenmodes according to Eq. (39) and then generate the corresponding dynamical matrix through $\mathbf{e}_{\mathcal{S}\mathbf{q}}D_{\mathbf{q}}^{\text{ph}}\mathbf{e}_{\mathcal{S}\mathbf{q}}^{\dagger}$, with $D_{\mathbf{q}}^{\text{ph}}$ being the diagonal matrix defined by Eq. (27) for the wave vector $\mathbf{q}$.

The transformation law of the phonon perturbation $\partial V_{\mathbf{q}\nu}(\mathbf{r})$ under the operation $\{\mathcal{S}|\mathbf{v}\}$ is most easily worked out by noting that (i) the displacement $\Delta\boldsymbol{\tau}_{\kappa p}^{\mathbf{q}\nu}$ [Eq. (12)] is both transferred to the atom $\kappa'=F_{\mathcal{S}}(\kappa)$ in the unit cell $\mathbf{R}_{p'}=\mathcal{S}\mathbf{R}_p$ and rotated according to $\mathcal{S}$:

$$\Delta\boldsymbol{\tau}_{\kappa'p'}^{\mathcal{S}\mathbf{q},\nu} = \mathcal{S}\Delta\boldsymbol{\tau}_{\kappa p}^{\mathbf{q}\nu}, \tag{41}$$

(ii) the dielectric function is invariant under the symmetry operation $\{\mathcal{S}|\mathbf{v}\}$:

$$\epsilon(\{\mathcal{S}|\mathbf{v}\}\mathbf{r},\quad \{\mathcal{S}|\mathbf{v}\}\mathbf{r}') = \epsilon(\mathbf{r},\mathbf{r}'), \tag{42}$$

and (iii) the ionic (pseudo)potentials are rotationally invariant:

$$V_\kappa^{\text{ion}}(\mathcal{S}\mathbf{r}) = V_\kappa^{\text{ion}}(\mathbf{r}). \tag{43}$$

By replacing Eqs. (41)–(43) into Eqs. (11)–(13), we obtain, after some algebra,

$$\partial V_{\mathcal{S}\mathbf{q}}(\mathbf{r}) = \partial V_{\mathbf{q}}(\{\mathcal{S}|\mathbf{v}\}^{-1}\mathbf{r}). \tag{44}$$

It is important to realize that the derivation of Eq. (44) rests on the choice of the phases of the vibrational eigenmodes at $\mathbf{q}$ and $\mathcal{S}\mathbf{q}$ provided by Eq. (39).

We can now exploit Eq. (44) to calculate the e-ph matrix element corresponding to a momentum transfer of $\mathcal{S}\mathbf{q}$:

$$g_{mn,\nu}(\mathbf{k},\mathcal{S}\mathbf{q}) = \langle\psi_{m\mathbf{k}+\mathcal{S}\mathbf{q}}(\mathbf{r})|\partial V_{\mathbf{q}}(\{\mathcal{S}|\mathbf{v}\}^{-1}\mathbf{r})|\psi_{n\mathbf{k}}(\mathbf{r})\rangle. \tag{45}$$

In a pseudopotential plane-wave formulation, if the electronic eigenfunctions $\psi_{n\mathbf{k}}(\mathbf{r})$ are expanded with a cutoff $E_{\text{kin}}$, the phonon perturbation will be expanded with a cutoff $4E_{\text{kin}}$ (this applies to norm-conserving pseudopotentials;[70] in the case of ultrasoft pseudopotentials,[71] the cutoff of the phonon perturbation would be larger because of the augmentation charge). Therefore, in such cases, it is more convenient to apply the symmetry operation $\{\mathcal{S}|\mathbf{v}\}$ to the electronic eigenfunctions rather than to the phonon perturbation. A simple change of variables in Eq. (45) gives

$$g_{mn,\nu}(\mathbf{k},\mathcal{S}\mathbf{q}) = \langle\psi_{m\mathbf{k}+\mathcal{S}\mathbf{q}}(\{\mathcal{S}|\mathbf{v}\}\mathbf{r})|\partial V_{\mathbf{q}}(\mathbf{r})|\psi_{n\mathbf{k}}(\{\mathcal{S}|\mathbf{v}\}\mathbf{r})\rangle. \tag{46}$$

At this point, it may be tempting to apply the same arguments discussed for the dynamical matrix to the electronic Hamiltonian to express $|\mathbf{k}+\mathcal{S}\mathbf{q}\rangle$ in terms of $|\mathcal{S}^{-1}\mathbf{k}+\mathbf{q}\rangle$:

$$\psi_{m\mathbf{k}+\mathcal{S}\mathbf{q}}(\{\mathcal{S}|\mathbf{v}\}\mathbf{r}) = \psi_{m\mathcal{S}^{-1}\mathbf{k}+\mathbf{q}}(\mathbf{r}). \tag{47}$$

However, Eq. (47) implicitly assumes a specific phase relation between electronic states at $\mathbf{k}+\mathcal{S}\mathbf{q}$ and $\mathcal{S}^{-1}\mathbf{k}+\mathbf{q}$, which, in general, does not hold if the gauge-fixing procedure described in Sec. V C has already been performed. For this reason, in our calculations, we determine the e-ph matrix elements directly through Eq. (45), which goes along with the phonon phase setting given by Eq. (39) but does not require Eq. (47) to be satisfied.

Of course, an alternative approach would be to enforce Eq. (47) from the very beginning in the gauge-fixing procedure described in Sec. V C. In both cases, the application of the symmetry operation $\{\mathcal{S}|\mathbf{v}\}$ to the electronic eigenfunctions is required. The computational cost of this step is negligible with respect to the determination of the dynamical matrix and the phonon perturbations for a given $\mathbf{q}$ vector.

## VI. APPLICATION TO BORON-DOPED DIAMOND

In order to illustrate the scheme developed in Secs. III and IV with a practical calculation, we present here an application to a virtual crystal model of B-doped diamond. We first provide the technical details of the calculation. Then, we discuss the localization properties of the Hamiltonian, the dynamical matrix and the e-ph vertex in the Wannier representation, and the ensuing accuracy of the Fourier interpolation in momentum space. Finally, we present our results for the electron and phonon self-energy arising from the e-ph interaction, for the Eliashberg function, and for the mass enhancement parameter.

### A. Technical details

Following Refs. 28 and 35, we consider B-doped diamond with a B content of 1.85%, which is close to the original experimental value.[33] The calculations are performed within the framework of density-functional theory in the local-density approximation.[72,73] We account for the core-valence interaction by using norm-conserving pseudopotentials.[70,74] Lattice-dynamical properties are calculated within density-functional perturbation theory with the method of Refs. 32 and 75 and maximally localized Wannier functions obtained by minimizing the Berry-phase spread functional with the method of Refs. 49, 53, and 64. The electronic wave functions are described by a plane-wave basis[63,76] with a kinetic energy cutoff of 60 Ry, yielding a total-energy accuracy of 10 meV/atom. The pseudopotential for the virtual atom $\mathrm{B}_x\mathrm{C}_{1-x}$, with $x=1/54=0.0185$, was generated by considering an ionic charge $Z^{\text{ion}}=3x+4(1-x)$ and the common core electron density of boron and carbon. The fractional occupations are described by first-order Hermite-Gaussian smearing.[77] We checked the convergence of the lattice constant with re-

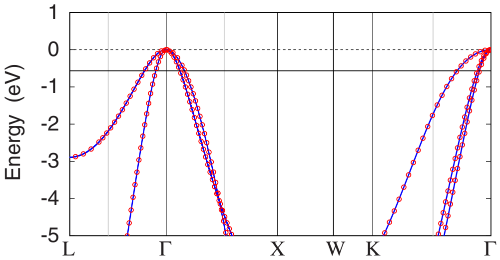

FIG. 3. (Color online) Comparison between the electronic band structure of pristine diamond (lines) and of B-doped diamond within a virtual crystal approximation (circles). The Fermi level of doped diamond with a B concentration of 1.85% is located 0.57 eV below the valence band top at Γ and is indicated by a black solid line.

spect to Brillouin-zone sampling and smearing parameter by considering uniform and unshifted Brillouin-zone grids with up to $20^3$ points and a broadening as small as 0.001 Ry. The converged lattice parameter was 6.6425 bohr (3.515 Å). The use of less stringent convergence parameters ($12^3$ **k** points and 0.05 Ry smearing) led to a lattice constant differing by less than 0.002% from the fully converged value. The calculated parameter underestimates the experimental lattice constant of 3.576 Å (Ref. 33)by 1.7%, consistent with the common trend observed within the local-density approximation. Since the B doping leads to the formation of a small Fermi surface centered at Γ (cf. Fig. 3), the zone-center phonons are the most sensitive to the metallic character of this system. Accordingly, we tested the convergence of the calculated vibrational frequencies for the highest optical modes at Γ. The converged frequency for a smearing of 0.02 Ry and a **k** point mesh of size $24^3$ was 138.7 meV. A smearing of 0.05 Ry together with a mesh of $12^3$ points yielded the very similar frequency of 139.3 meV. For convenience, in the following, we describe results obtained within the latter settings.

Figure 3 shows the calculated band structure of B-doped diamond compared to the band structure of pristine diamond. The calculation for pristine diamond was performed with the same lattice parameter of the doped system for the purpose of comparison (the relaxed lattice parameter of B-doped diamond with a B content of 2% is 0.2% larger than that of intrinsic diamond). After aligning the top of the valence bands, the one-particle eigenvalues corresponding to the occupied subspace are found to differ by 0.1 eV at most, indicating that the effect of the virtual pseudopotential could be simulated equally by a simple rigid band model. The Fermi level in of B-doped diamond is located 0.57 eV below the top of the valence bands, which is in good agreement with previous theoretical studies.[28]

Figure 4 shows the calculated phonon dispersions of B-doped diamond, together with the phonon dispersions of pristine diamond with the same lattice parameter. Within the virtual crystal approximation, the doping with boron induces a softening of the optical phonon frequencies around the zone center. The largest softening is observed at the Γ point and amounts to 28 meV. This value severely overestimates the experimentally measured softening of 7 meV,[78] indicating that a virtual crystal approximation is not sufficient to describe the lattice dynamics of B-doped diamond.[35]

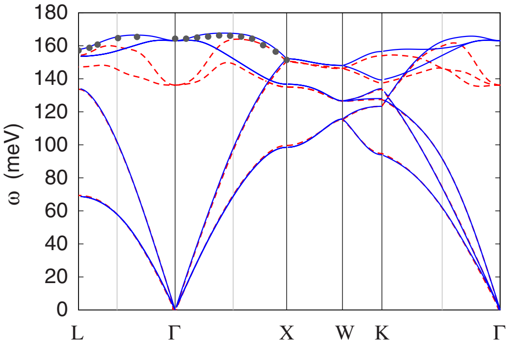

FIG. 4. (Color online) Comparison between the phonon dispersions of pristine diamond (solid lines) and B-doped diamond within a virtual crystal approximation (dashed lines). The disks correspond to inelastic neutron scattering data from Ref. 79.

### B. Wannier representation and interpolation

In order to determine the electronic states in the Wannier representation, we need to define an appropriate energy subspace for projecting the electronic Hamiltonian. The identification of this subspace is particularly simple in the present case, since (i) boron doping shifts the Fermi down into the valence bands of diamond. (ii) As discussed in Sec. II, only electronic states close to the Fermi level need to be considered to compute the phonon linewidths, and only electronic states with energy close to the initial state $\epsilon_{n\mathbf{k}}$ are required for the electron linewidths. (iii) The (local-density approximation) indirect band gap of intrinsic diamond is 4.3 eV; therefore, the electronic transitions from the valence to the conduction bands do not contribute to the electron and phonon linewidths nor to the superconducting pairing. Following these considerations, we choose to describe the electronic structure of B-doped diamond by considering four bond-centered Wannier functions spanning the four valence bands of diamond.[49] The maximally localized Wannier functions corresponding to this choice exhibit a spatial spread of 0.85 Å.

Figure 5 shows the spatial decay of the Hamiltonian matrix elements in the Wannier representation $H^{\mathrm{el}}_{\mathbf{R}_e,\mathbf{R}'_e}$ as a function of the distance between the unit cells $\mathbf{R}_e,\mathbf{R}'_e$ in which the Wannier functions are located. The Hamiltonian matrix elements are already very small for next-nearest-neighbor Wannier functions (the reduction is approximately a factor of 0.01). This finding is consistent with the proved accuracy of nearest-neighbor tight-binding parametrizations of the electronic structure of carbon-based systems.[80] The exponential decay of the Hamiltonian matrix elements reflects the exponential localization of Wannier functions corresponding to the bonding orbitals of diamond. The present case is particularly favorable since the hole doping preserves much of the band structure of the insulating system: there is no entanglement with higher-energy states, and we effectively deal with a composite group of bands.

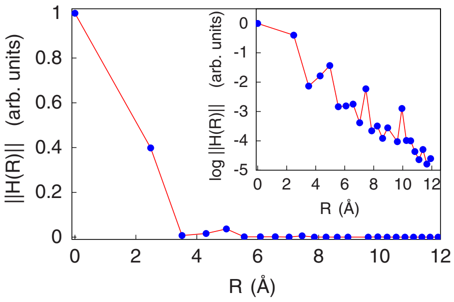

FIG. 5. (Color online) Spatial decay of the electronic Hamiltonian in the Wannier representation $H^{\rm el}_{\mathbf{R}_e,\mathbf{R}'_e}=\langle m\mathbf{R}'_e|\hat{H}^{\rm el}|n\mathbf{R}_e\rangle$ [Eq. (26)] as a function of $R=|\mathbf{R}_e-\mathbf{R}'_e|$. The data points correspond to the largest value taken over the Wannier functions indices and over the unit cells $\mathbf{R}_e$, $\mathbf{R}'_e$ located at the same distance $R$: $\|H(R)\|=\max_{mn,|\mathbf{R}_e-\mathbf{R}'_e|=R}|\langle m\mathbf{R}'_e|\hat{H}^{\rm el}|n\mathbf{R}_e\rangle|$. The data are normalized to their largest value. The inset shows the same quantity on a logarithmic scale ($\log_{10}$).

Figure 6 shows the spatial decay of the phonon dynamical matrix in the Wannier representation [Eq. (29)]. It is well known that the interatomic force constants of intrinsic diamond exhibit a rather fast spatial decay because of the vanishing Born dynamical charges (the first nonzero contribution is a quadropole-quadrupole interaction). In the case of B-doped diamond considered here, the metallic screening produces a softening of the phonons around the zone center. However, this does not significantly alter the range of the interatomic force constants with respect to intrinsic diamond. Accordingly, for the lattice-dynamical matrix, we also observe exponential localization.

After having examined the spatial decay of the Hamiltonian and the dynamical matrix, we now turn to the e-ph matrix element $g(\mathbf{R}_e,\mathbf{R}_p)$ (Fig. 7). In this case, we have two spatial variables and it is convenient to restrict the discussion to the limiting cases considered in Sec. III C: (i) $\mathbf{R}_p=\mathbf{0}$, when the localized phonon perturbation and one Wannier function are located within the same unit cell, and (ii) $\mathbf{R}_e=\mathbf{0}$, when the two electron Wannier functions belong to the same unit cell. In the first case, the spatial decay is dictated by the localization of electronic Wannier functions and is expected to be similar to the decay of the Hamiltonian matrix elements in the Wannier representation. Figure 7(a) shows that this is indeed the case since we observe exponential decay in the electronic variable $\mathbf{R}_e$. In the second case, the spatial decay of $g(\mathbf{0}_e,\mathbf{R}_p)$ with $\mathbf{R}_p$ directly reflects the decay of the phonon perturbation in the Wannier representation and is expected to exhibit a localization similar to the dynamical matrix (cf. Sec. III C). Figure 7(b) shows that the e-ph matrix elements decay rather quickly (within next-nearest-neighbor distances), although the decay rate is smaller than for the force constants. This is consistent with the fact that the force constants relate to the *gradient* of the phonon perturbation [cf. Eq. (19)].

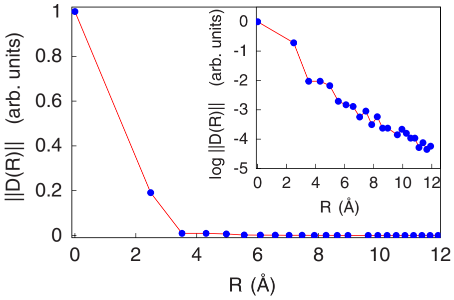

FIG. 6. (Color online) Spatial decay of the dynamical matrix in the Wannier representation $D^{\rm ph}_{\mathbf{R}_p,\mathbf{R}'_p}=\langle\mathbf{R}_p|\hat{D}^{\rm ph}|\mathbf{R}'_p\rangle$ [Eq. (29)] as a function of the distance $R=|\mathbf{R}_p-\mathbf{R}'_p|$. The data points correspond to the largest value taken over the ions in the unit cell, the Cartesian directions, and the unit cells $\mathbf{R}_p$, $\mathbf{R}'_p$ located at the same distance $R$: $\|D(R)\|=\max_{\kappa\kappa'\alpha\alpha',|\mathbf{R}_p-\mathbf{R}'_p|=R}|\langle\kappa'\alpha'\mathbf{R}_p|\hat{D}^{\rm ph}|\kappa\alpha\mathbf{R}'_p\rangle|$. The data are normalized to their largest value. The inset shows the same quantity on a logarithmic scale ($\log_{10}$).

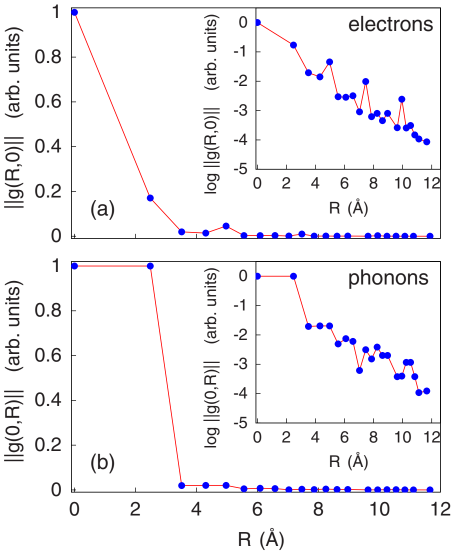

FIG. 7. (Color online) Spatial decay of the e-ph vertex in the joint electron-phonon Wannier representation $g_{mn,\nu}(\mathbf{R}_e,\mathbf{R}_p)=\langle m\mathbf{0}_e|\partial_{\kappa\alpha,\mathbf{R}_p}V|n\mathbf{R}_e\rangle$ [Eq. (23)] as a function of $\mathbf{R}_p$ and $\mathbf{R}_e$: (a) the limiting case $g(\mathbf{R}_e,\mathbf{R}_p=\mathbf{0})$ and (b) the limiting case $g(\mathbf{R}_e=\mathbf{0},\mathbf{R}_p)$. The data points correspond to the largest value taken over the Wannier functions indices, the ions in the unit cell, the Cartesian directions, and the unit cells located at the same distance $R=|\mathbf{R}_e|$ [panel (a)] or $R=|\mathbf{R}_p|$ [panel (b)] from the origin of the reference frame: (a) $\|g(R,0)\|=\max_{mn,\kappa\alpha,|\mathbf{R}_e|=R}|g_{mn,\kappa\alpha}(\mathbf{R}_e,\mathbf{0}_p)|$ and (b) $\|g(0,R)\|=\max_{mn,\kappa\alpha,|\mathbf{R}_p|=R}|g_{mn,\kappa\alpha}(\mathbf{0}_e,\mathbf{R}_p)|$. The data are normalized to their largest value. The insets show the same quantities on a logarithmic scale ($\log_{10}$). When two Wannier functions are located on a C–C bond crossing a cell boundary, identical e-ph matrix elements appear in adjacent unit cells, resulting in the steplike behavior seen in (b).

In order to have an idea of the Brillouin-zone sampling required to obtain matrix elements encompassing a given spatial range $R$, we notice that in the present case, a uniform $6\times6\times6$ sampling corresponds to interactions extending up to $R\sim10$ Å, while a grid with $12\times12\times12$ **k** points in the Brillouin zone corresponds to a maximum range of $R\sim20$ Å. Hence, Figs. 5–7 indicate that a Brillouin-zone sampling corresponding to a $6\times6\times6$ supercell should be sufficient to determine the self-energies [Eqs. (3) and (4)] with an accuracy of 1% [without taking into account cancellation of errors arising from the **k** and **q** integrations in Eqs. (3) and (4)]. In the following section, we verify this observation by comparing the e-ph matrix elements obtained by the Wannier-Fourier interpolation method discussed in Sec. IV with those computed directly from first principles.

### *Accuracy of the electron-phonon matrix elements*

In order to assess the accuracy of the interpolation method introduced in Sec. IV, we need to compare the various quantities needed for studying the e-ph interaction (single-particle electronic eigenvalues, vibrational frequencies, and e-ph matrix elements) obtained by Wannier-Fourier interpolation with those obtained directly from first principles. The interpolation procedures for the band structure and for the phonon dispersions have already been addressed elsewhere;[32,53,58] therefore, we restrict ourselves here to the e-ph matrix elements.

The e-ph vertex $g_{mn,\nu}(\mathbf{k},\mathbf{q})$ is a ten-dimensional object, and it is hard to present a comprehensive visual comparison of the *ab initio* and the interpolated matrix elements. We focus here on a special case which is representative of the general trend. For this purpose, we take the initial electronic state $|n\mathbf{k}\rangle$ to be the $\Gamma'_{25}$ state (top of the valence band at the zone center), and we vary the phonon momentum **q** along the same high-symmetry lines $\Lambda$, $\Delta$, and $\Sigma$ considered in Figs. 3 and 4. For each phonon momentum, the final electronic state $|m\mathbf{k}+\mathbf{q}\rangle$ is taken on the top of the valence manifold through the twofold degenerate bands $\Lambda_3$ and $\Delta_5$, as well as the nondegenerate $\Sigma_2$ band [Fig. 8(a), dashed line]. The emitted and/or absorbed phonon is taken to be the highest optical mode at the given momentum **q** along the same symmetry lines, with the exception of the $\Sigma$ line where we pick the $\Sigma_1$ branch rather than the highest-energy $\Sigma_3$ branch [Fig. 8(b), dashed line]. These choices were made in order to avoid symmetry-forbidden transitions which are uninteresting for our comparison. As discussed is Sec. V C, the e-ph matrix element is not gauge invariant; therefore, the matrix elements corresponding to degenerate electronic or vibrational states do not carry any physical meaning by themselves. However, for illustration purposes, we adopt here the convention that every individual (squared) matrix element corresponds to the average within the eventual degenerate manifold. This convention leads to a discontinuity of the e-ph matrix elements at the zone center which can be observed in Fig. 8(c).

Figure 8(c) shows the variation of the e-ph matrix element along the described energy and/or momentum path, as computed directly from first principles, together with the values obtained by the joint electron-phonon interpolation procedure outlined in Sec. IV. We considered 50 phonon momenta in the *ab initio* calculation and unshifted Brillouin-zone grids with $4^3$, $6^3$, or $8^3$ points for the interpolation procedure (we generated 500 phonon momenta on the high-symmetry lines considered in Fig. 8). The calculated e-ph matrix elements are consistent with the electron-phonon potential $V_{\mathrm{ep}}=280$ meV obtained in Ref. 28, as well as the average matrix element $\langle|g|^2\rangle^{1/2}=670$ meV estimated in Ref. 36 by deformation potential calculations. However, contrary to previous assumptions,[28,36] the e-ph *vertex varies significantly throughout the Brillouin zone*, ranging from 0 to ~500 meV.

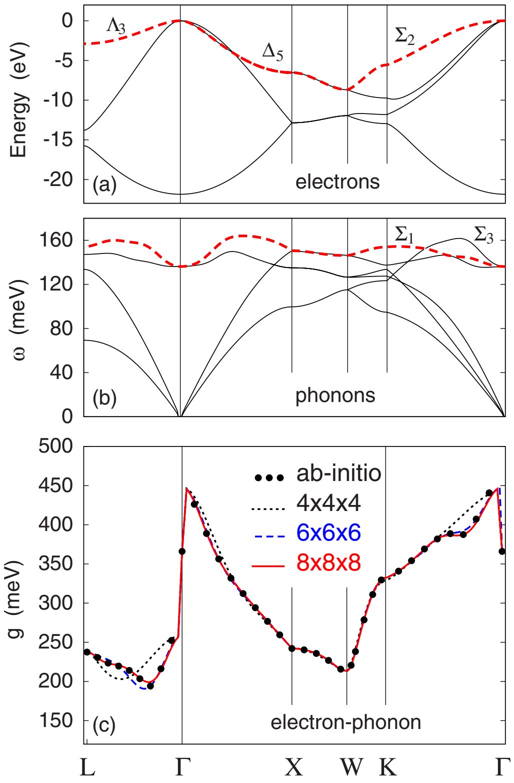

FIG. 8. (Color online) Comparison of the e-ph matrix elements $g^{\mathrm{SE}}_{mn,\nu}(\mathbf{k},\mathbf{q})$ [Eq. (5)] obtained by direct first-principles calculations [panel (c), disks] and those computed with the Wannier-Fourier interpolation method discussed in Sec. IV [panel (c), lines]. The interpolated matrix elements are computed starting from an initial $4^3$ Brillouin-zone grid (dotted line), a $6^3$ grid (dashed line), or a $8^3$ grid (solid line). For illustration, we fixed the initial electronic state $|n\mathbf{k}\rangle$ for the valence band top at $\Gamma$ $(\mathbf{k}=\mathbf{0})$; we let the final electronic state $|m\mathbf{k}+\mathbf{q}\rangle$ span the $\Lambda_3$, $\Delta_5$, and $\Sigma_2$ bands as shown in panel (a) (dashed line), and we take the phonon perturbation corresponding to the highest optical branches as shown in panel (b) (dashed line).

It is clear that our interpolation scheme is very effective, and already a $6\times6\times6$ grid provides a very accurate description of the electron-phonon interaction in the example considered. We notice that the initial dynamical matrices and phonon perturbations for $6\times6\times6$ phonon momenta are obtained from the irreducible wedge of the Brillouin zone and therefore correspond to only 16 separate calculations.

For a quantitative assessment of the accuracy of our method, we report here the absolute deviations of the interpolated e-ph matrix elements with respect to the first-principles calculations on a uniform Brillouin-zone grid with $10^3$ points. We found the largest deviations of 80, 30, and 15 meV for initial Brillouin-zone grids containing $4^3$, $6^3$, and $8^3$ points, respectively. The corresponding deviations for the interpolated electronic eigenvalues were 0.5, 0.1, and 0.05 eV, respectively, while the deviations of the phonon frequencies were 10, 2, and 1 meV, respectively.

At the end of this section, it is worth pointing out that, compared to other possible interpolation schemes, the one discussed in the present work relies on a physical property of the system, which could be designated as the "nearsightedness" of the electron-phonon interaction, in analogy with a very general concept introduced for the electron-electron interaction.[81] In favorable cases (such as the application discussed here), our scheme shows *exponentially increasing accuracy* with the spacing of the coarse grid on which the first-principles calculations are performed.

### C. Electron and phonon linewidths, Eliashberg function, and mass enhancement parameter

Once the accuracy of the Wannier-Fourier interpolation is established, we proceed to investigate the convergence of the electron and phonon linewidths [Eqs. (3) and (4)] with the sampling of the Brillouin zone. All the calculations described in this section were performed by interpolating the electron Hamiltonian, the lattice-dynamical matrix, and the e-ph vertex evaluated on the unshifted $8^3$ grid discussed in Sec. VI B. The Dirac delta functions in Eqs. (3) and (4) were replaced by Lorentzian distributions. The Fermi-Dirac and Bose-Einstein occupations in Eqs. (3) and (4) were calculated with the temperature set to 300 K.

#### *1. Electron linewidths*

Figure 9 shows the calculated electron linewidths arising from the e-ph interaction for the electronic states indicated in Fig. 8 ($\Lambda_3$ and $\Delta_5$ bands). The linewidths corresponding to the other bands close to the Fermi level have qualitatively similar behavior. The integration over the phonon momentum in Eq. (3) is performed by interpolating the matrix elements on two sets of Brillouin-zone meshes: a coarse grid including $10\times10\times10$ points in the *irreducible wedge*, obtained by randomly shifting a uniform grid, as well as a fine grid including $50\times50\times50$ points in the irreducible wedge. For each Brillouin-zone mesh, we repeated the calculations by setting the Lorentzian half-width to 10, 50, and 100 meV, respectively. Figure 9 shows that 1000 $\mathbf{q}$ points are not sufficient to perform the momentum integration. The use of a small smearing parameter [10 meV, Fig. 11(a)] leads to strong fluctuations of the linewidths, making it difficult to identify a clear trend. On the other hand, a large smearing [100 meV Fig. 11(c)] increases the linewidths close to the zone center, leading to unphysical results (*vide infra*). The calculations performed with 125 000 $\mathbf{q}$ points in the momentum integration is found to produce reasonably good results for the smallest smearing considered of 10 meV [Fig. 11(c)], although small unphysical fluctuations still persist.

It is worth mentioning that most current calculations of the e-ph interaction are performed with grids including considerably fewer irreducible phonon momenta, since the direct computation of the lattice-dynamical matrix corresponds to several total-energy minimizations for each $\mathbf{q}$ point. In practice, without our Wannier-Fourier technique, the calculations described here would require several months of computation on modern computers.[82]

The calculated electron linewidths show a peculiar suppression when the electron momentum lies close to the zone center. Careful analysis indicates that this happens for all electronic states with energy $\epsilon_{n\mathbf{k}}$ within $\omega^{\rm op}$ from the valence band top at $\Gamma$, where $\omega^{\rm op}\simeq 160$ meV is a characteristic optical phonon frequency. In this case, the electron cannot emit a phonon since there are no available final states at the energy $\epsilon_{n\mathbf{k}}+\omega^{\rm op}$ [the final state falls within the band gap, cf. Eq. (3)]. Within this energy range, it is still possible for an electron to emit an acoustic phonon; however, the matrix element for this process is practically negligible. For electronic states far from the zone center, we observe a monotonic increase of the linewidth with the electron momentum. This behavior can be understood by considering Eq. (3). If we replace the e-ph matrix element by its average value throughout the Brillouin zone and remember that we are considering occupied states, the imaginary part of the self-energy becomes $|\Sigma''_{n\mathbf{k}}| \simeq \pi\Omega_{\rm BZ}^{-1}|g^{\rm SE}|^2\Sigma_{m\nu}\int_{\rm BZ}d\mathbf{q}\,\delta(\epsilon_{n\mathbf{k}}-\omega_{\mathbf{q}\nu}-\epsilon_{m\mathbf{k}+\mathbf{q}})$. By neglecting the phonon frequency in the delta function, we obtain the electronic density of states at the energy of the initial state $N(\epsilon_{n\mathbf{k}})$. Therefore, when we move off the $\Gamma$ point, the linewidth increases following the density of states. We have checked numerically that the electron linewidth scales as $|\Sigma''(\omega)|\sim\omega^{1/2}$, which is consistent with the underlying density of states of the parabolic bands of diamond. We notice that this behavior is at variance with common models of the electron self-energy arising from the e-ph interaction.[38] The latter models are based on the assumption of a constant density of states around the Fermi level, which does not hold in the present case. The calculated linewidths for electronic

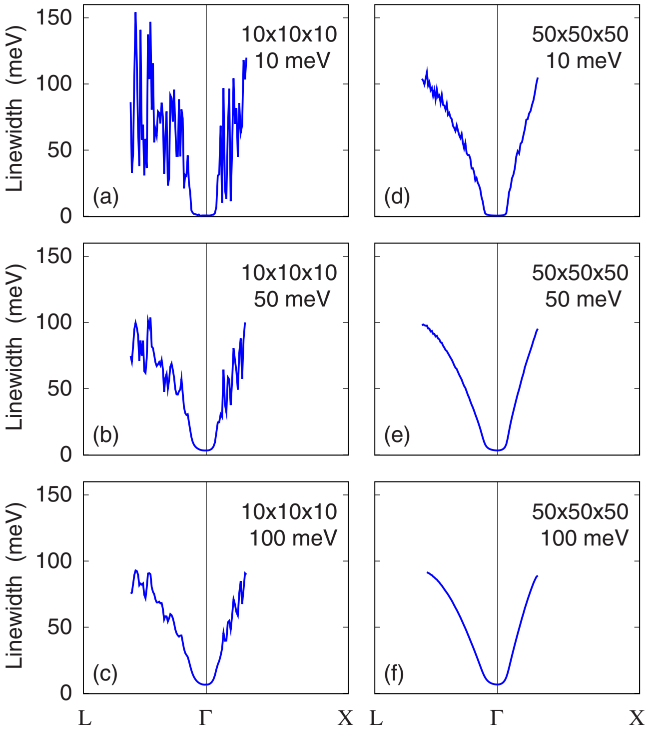

FIG. 9. (Color online) Calculated electron linewidths for the $\Lambda_3$ and $\Delta_5$ bands of B-doped diamond [Fig. 8(a)]. Plots (a)–(c) on the left were obtained by using $10^3$ irreducible $\mathbf{q}$ points in the momentum integration of Eq. (3), while plots (d)–(f) on the right were obtained with $50^3$ irreducible points in the Brillouin zone. We report the results for three broadening parameters $\eta$: 10 meV [panels (a) and (d)], 50 meV [panels (b) and (e)], and 100 meV [panels (c) and (f)]. The curves are cut off at half the Brillouin-zone size for clarity.

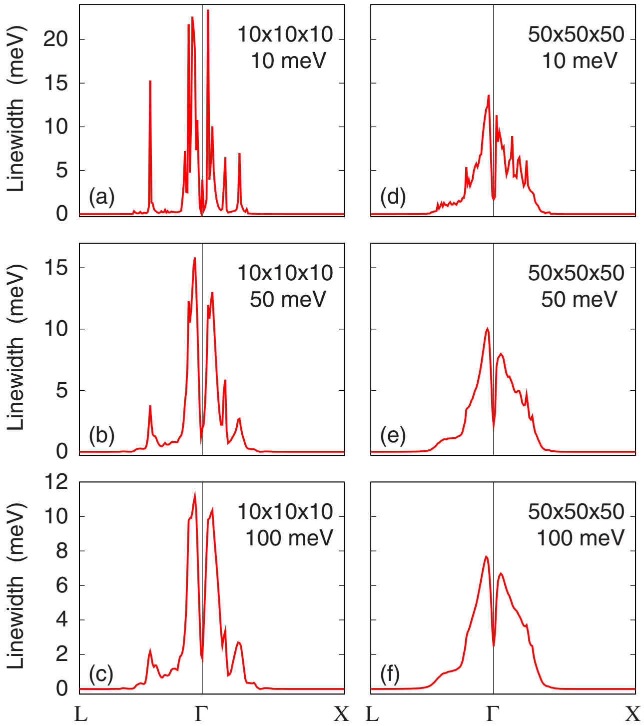

FIG. 10. (Color online) Calculated phonon linewidths for the highest optical mode of B-doped diamond [Fig. 8(b)]. Plots (a)–(c) on the left were obtained with $10^3$ irreducible **q** points in the momentum integration of Eq. (4), while plots (d)–(f) on the right were obtained with $50^3$ irreducible points. The results for three broadening parameters 10, 50, and 100 meV are shown in panels (a) and (d), panels (b) and (e), and panels (c) and (f), respectively. Note the different vertical scales in the plots corresponding to different broadening parameters.

states close to the Fermi level (~50 meV) are smaller than the values of ~300 meV that can be estimated from the photoemission data of Ref. 83. The underestimation of the experimental widths is consistent with the fact that our theory does not take into account the broadening induced by electron-electron and the electron-dopant interactions.

### 2. Phonon linewidths

Figure 10 shows the phonon linewidths corresponding to the longitudinal optical mode of B-doped diamond [cf. 8(b)] calculated with different Brillouin-zone grids and smearing parameters. The transverse optical modes behave similarly, while the linewidths associated with the acoustic modes were found to be negligibly small (less than 0.5 meV throughout the entire Brillouin zone). We find that 1000 **q** points in the irreducible zone are not sufficient to reproduce the correct momentum dependence of the phonon linewidths. On the other hand, a Brillouin-zone mesh with 125 000 **q** points yields reasonably good results, although small unphysical fluctuations can still be seen in the plots. Two features stand out in the plots of Fig. 10: (i) the linewidths become negligible as we move far enough from the zone center, and (ii) there is singular behavior at the zone-center where we observe a dip instead of a peak. Feature (i) is associated with the fact that phonons with momentum larger than the average

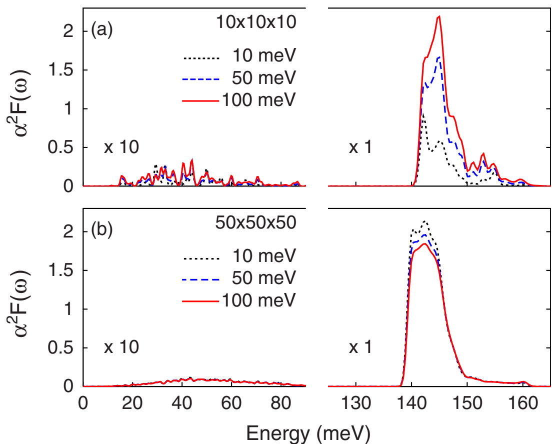

FIG. 11. (Color online) Eliashberg function $\alpha^2F(\omega)$ calculated for B-doped diamond in the virtual crystal approximation with (a) $10^3$ **k** and **q** points in the irreducible part of the Brillouin zone and (b) $50^3$ points. For each case, we report the results corresponding to the smearing parameters 10 meV (dotted lines), 50 meV (dashed lines), and 100 meV (solid lines). The Dirac delta function in Eq. (7) was replaced by a Gaussian with a standard deviation of 0.5 meV. Note the different energy scales and scaling factors for the acoustic and the optical frequency ranges.

Fermi-surface diameter ($q>2k_F$) cannot be scattered since the initial and final electronic states are pinned near to the Fermi surface [cf. Eq. (4)].[35] Feature (ii) is more subtle and arises from the fact that electronic transitions with no momentum transfer ($\mathbf{q}=\mathbf{0}$) are essentially forbidden. When the energy separation between initial states on the Fermi surface and final states with the same momentum **k** exceeds the largest phonon frequency $\omega^{\mathrm{op}}$, the transition is blocked by the energy selection rule in Eq. (4).[35,46] Our linewidths are consistent with those calculated in Ref. 84. However, the characteristic dip at the zone center found here is missing in Ref. 84 because of the common although unjustified approximation of neglecting of the phonon energy in Eq. (4).

In Fig. 10, the linewidths close to the zone center are consistent with the values of ~8 meV determined by inelastic x-ray scattering on B-doped diamond samples with a similar doping level.[78] We note, however, that in the present work, we do not take into account the local structural relaxation induced by the B atoms. When this effect is included, finite phonon linewidths are observed even at large momenta ($q>2k_F$) due to the breaking of the lattice periodicity.[35]

### 3. Eliashberg function and mass enhancement parameter

Figure 11 shows the Eliashberg function [Eq. (7)] obtained with the phonon linewidths discussed in Sec. VI C 2. As already pointed out, 1000 **k** and **q** irreducible points in the Brillouin zone are not sufficient to achieve convergence, while a grid with 125 000 points leads to stable results. The reliability of the calculated Eliashberg function is important in the study of phonon-mediated superconductivity, since $\alpha^2F(\omega)$ is commonly used to identify the phonon modes responsible for the pairing. Figure 11 shows that, within the

TABLE II. Electron-phonon mass enhancement parameter $\lambda$ of B-doped diamond in the virtual crystal approximation, calculated with different Brillouin-zone grids and smearing parameters.

| | 10 meV | 50 meV | 100 meV |
|---|---|---|---|
| $10\times10\times10$ | 0.073 | 0.156 | 0.212 |
| $50\times50\times50$ | 0.232 | 0.219 | 0.210 |

virtual crystal approximation, only the high-frequency optical modes of B-doped diamond participate in the superconducting pairing, while the acoustic modes play a minor role. When the dopant atoms are taken explicitly into account,[28,35] the picture derived from the virtual crystal model needs to be revised; the dominant contribution to the pairing field is found to arise from the vibrational modes associated with the impurity.[28,35]

The mass enhancement parameter $\lambda$ is obtained from the Eliashberg function through Eq. (8). This parameter is commonly used to estimate the superconducting transition temperature of isotropic superconductors in conjunction with the semiempirical McMillan formula $T_c=\frac{\omega_{\log}}{1.2}\exp\{-1.04(1+\lambda)/[\lambda-\mu^\star(1-0.62\lambda)]\}$, where $\omega_{\log}$ is the logarithmic averaged phonon frequency and $\mu^\star$ is the Coulomb pseudopotential.[85] Since the superconducting transition temperature exhibits an exponential dependence on $\lambda$ (at least for $\lambda \lesssim 1.25$), it is essential to obtain accurate values for the coupling strength. A survey of the existing literature reveals that calculated values of $\lambda$ for B-doped diamond vary by more than a factor of 2, ranging from $\lambda=0.24$ to $\lambda=0.53$.[28,36,37,84,86] The superconducting transition temperature $T_c$ corresponding to this range (assuming, for simplicity, the same Coulomb pseudopotential $\mu^\star=0.13$ and the logarithmic frequency $\omega_{\log}=1000\ \mathrm{cm}^{-1}$) spans several orders of magnitude, from $10^{-3}$ to 14 K, clearly pointing to a serious difficulty in the calculation of e-ph interaction properties.

Table II reports our calculated e-ph coupling strengths corresponding to the Eliashberg functions shown in Fig. 11. We find that a grid of 1000 points in the irreducible wedge of the Brillouin zone yields $\lambda$ values which are very sensitive to the choice of the smearing parameter. A grid with 125 000 points provides instead results which are reasonably insensitive to this choice. Our fully converged value for the e-ph coupling strength is $\lambda=0.237$. This value was obtained in Ref. 35 using $100^3$ $\mathbf{k}$ points and $30^3$ $\mathbf{q}$ points in the irreducible wedge of the Brillouin zone. The corresponding transition temperature is $5\times10^{-4}$ K (with a Coulomb pseudopotential $\mu^\star=0.13$ and a logarithmic frequency $\omega_{\log}=1010\ \mathrm{cm}^{-1}$) and is in sharp contrast with the experimentally observed $T_c$ of 4 K.[33] As discussed in Ref. 35, the failure of the virtual crystal model of B-doped diamond is to be ascribed to the neglect of the vibrational modes associated with the boron atoms.

## VII. CONCLUSION

The present work was motivated by the long-standing difficulty of studying the electron-phonon interaction from first principles. This difficulty arises from the necessity of a very careful description of the e-ph scattering processes in the Brillouin zone, in particular, in proximity of the Fermi surface. We have shown that this difficulty can be overcome by performing a generalized Wannier-Fourier interpolation of the e-ph vertex, leading to results as accurate as a full *ab initio* calculation but at a comparably negligible computational cost. In order to assess the accuracy of our methodology, we have performed a comprehensive set of tests on a virtual crystal model of B-doped diamond. In particular, we calculated the electron and phonon linewidths arising from the e-ph interaction as well as the Eliashberg spectral function, and we discussed the dependence of these quantities on the sampling of the Brillouin zone. Our study revealed that, contrary to common assumptions, the momentum dependence of the e-ph matrix element is significant throughout the Brillouin zone and cannot be neglected.

It is interesting to consider future directions and possible developments of the present theory. The first obvious application of our method consists in using the e-ph matrix elements in the Wannier representation to investigate how electrons and ions interact at the atomistic scale. Indeed, we could decompose the various contributions to the electron and phonon self-energies into their atomistic components in the spirit of the analysis of Ref. 56.

A further step in the same direction could be taken by reformulating the electron-phonon problem in a fully localized representation based on Wannier functions. This possibility is appealing since, as we have shown in this work, all the information needed to describe the e-ph interaction is encoded in a small number of matrix elements in the Wannier representation. Therefore, in principle, there is no need to go back to Bloch space by Wannier-Fourier interpolation. It is interesting to note that a similar idea has been suggested in Ref. 87, where the authors were interested in reformulating the Eliashberg equations in a localized Wannier representation.

Even without attempting an all-Wannier calculation as suggested above, our Wannier-Fourier interpolation method will prove useful for solving the Eliashberg equations appearing in the theory of strong-coupling superconductivity,[23,24,26] or the Bogoliubov–de Gennes-type equations to be solved in the density-functional theory for superconductors.[31,47] In both cases, a very fine description of the e-ph scattering processes near the Fermi surface is strictly required.

The availability of electron and phonon eigenstates and the associated e-ph matrix elements at a very small computational cost could also be used as a starting point to explore the effects of the vertex corrections to the Migdal approximation. Indeed, while, in principle, Migdal theorem does not apply in the presence of Fermi-surface nesting,[26] we are not aware of any attempts to go beyond this approximation within first-principles approaches.

Finally, we mention the possibility of using the present method to directly address the e-ph interaction in complex systems with many atoms in the unit cell,[35] or to define tight-binding parametrizations for large-scale systems.

## ACKNOWLEDGMENTS

We wish to thank J. R. Yates and I. Souza for their contribution to the initial stages of this work. In particular, we acknowledge J. R. Yates for providing a preliminary interface between the PWSCF and the WANNIER computer codes and I. Souza for useful discussions on the Wannier interpolation of electronic band structures. We also wish to thank C.-H. Park and J. Noffsinger for extensively testing the methodology presented in this work and S. De Gironcoli and X. Blase for fruitful interactions. This work was supported by the National Science Foundation Grant No. DMR04-39768 and by the Office of Science, Office of Basic Energy Sciences, Materials Sciences and Engineering Division, U. S. Department of Energy under Contract No. DE-AC02-05CH11231. Computational resources were provided by NPACI and NERSC. Part of the calculations were performed using the QUANTUM-ESPRESSO[75] and WANNIER[64] packages.

## APPENDIX: FOURIER INTERPOLATION OF THE SQUARED MATRIX ELEMENT

For completeness, in this appendix, we provide a formal justification of the approach proposed in Ref. 35. The procedure introduced in Ref. 35 is similar in spirit to the present work, altough the practical implementation differs considerably. Maintaining the notation of Sec. IV, the squared e-ph matrix element in the Bloch representation introduced in Ref. 35 is

$$g^2_{mn,\mu\nu,\mathbf{k}}(\mathbf{q}) = g^*_{mn,\mu}(\mathbf{k},\mathbf{q})\, g_{mn,\nu}(\mathbf{k},\mathbf{q}), \tag{A1}$$

while the corresponding matrix element in the phonon Wannier representation is

$$g^2_{mn,\mu\nu,\mathbf{k}}(\mathbf{R}_p) = \sum_{\mu'\nu'}\sum_{\mathbf{q}} e^{-i\mathbf{q}\cdot\mathbf{R}_p} u_{\mathbf{q}\mu\mu'}\, g^2_{mn,\mu'\nu',\mathbf{k}}(\mathbf{q})\, u^{-1}_{\mathbf{q}\nu'\nu}. \tag{A2}$$

The interpolation formula for an arbitrary phonon momentum $\mathbf{q}$ given in Ref. 35 is

$$g^2_{mn,\mu\nu}(\mathbf{k},\mathbf{q}) = \sum_{\mu'\nu'}\sum_{\mathbf{R}_p} e^{i\mathbf{q}\cdot\mathbf{R}_p} u^{-1}_{\mathbf{q}\mu\mu'}\, g^2_{mn,\mu'\nu',\mathbf{k}}(\mathbf{R}_p)\, u_{\mathbf{q}\nu'\nu}. \tag{A3}$$

The interpolation by means of Eq. (A3) is convenient when the matrix elements $g^2_{mn,\mu\nu,\mathbf{k}}(\mathbf{R}_p)$ exhibit a rapid spatial decay in the variable $\mathbf{R}_p$. We show here that the latter requirement follows from the localization of the phonon perturbation in the Wannier representation [Eq. (18)]. For this purpose, we consider the product $g(\mathbf{k},\mathbf{q})u^{-1}_{\mathbf{q}}$ in Eq. (A2). By combining Eqs. (15) and (6) we find

$$\sum_{\nu'} g_{mn,\nu'}(\mathbf{k},\mathbf{q})\, u^{-1}_{\mathbf{q}\nu'\nu} = \sum_{\mathbf{R}_p} e^{i\mathbf{q}\cdot\mathbf{R}_p}\langle m\mathbf{k}+\mathbf{q}|\partial_{\nu,\mathbf{R}_p}V|n\mathbf{k}\rangle. \tag{A4}$$

By changing the integration variable to $\mathbf{r}-\mathbf{R}_p$ and taking into account the resulting Bloch phases of $|m\mathbf{k}+\mathbf{q}\rangle$ and $|n\mathbf{k}\rangle$, we can rewrite Eq. (A4) as

$$\sum_{\nu'} g_{mn,\nu'}(\mathbf{k},\mathbf{q})\, u^{-1}_{\mathbf{q}\nu'\nu} = N_p\langle m\mathbf{k}+\mathbf{q}|\partial_{\nu,\mathbf{0}_p}V|n\mathbf{k}\rangle. \tag{A5}$$

It is convenient to Fourier analyze the potential $\partial_{\nu,\mathbf{0}_p}V$ as follows:

$$\partial_{\nu,\mathbf{0}_p}V(\mathbf{r}) = \int \partial V_\nu(\mathbf{q}')\, e^{i\mathbf{q}'\cdot\mathbf{r}}\, d\mathbf{q}', \tag{A6}$$

with the integration extending over the entire reciprocal space. We now combine Eqs. (A5) and (A6), decompose the real-space integral into a sum over $N_e$ unit cell integrals, and use the periodicity of the Bloch functions. The algebra shows that only the $\mathbf{q}$ wave component of $\partial_{\nu,\mathbf{0}_p}V(\mathbf{r})$ appears in the final expression:

$$\sum_{\nu'} g_{mn,\nu'}(\mathbf{k},\mathbf{q})\, u^{-1}_{\mathbf{q}\nu'\nu} = N_e N_p\, \partial V_\nu(\mathbf{q})\langle u_{m\mathbf{k}+\mathbf{q}}|u_{n\mathbf{k}}\rangle, \tag{A7}$$

where $u_{n\mathbf{k}}$ and $u_{m\mathbf{k}+\mathbf{q}}$ are the cell-periodic part of the electron Bloch functions, and the overlap integral is restricted to the unit cell. By combining Eqs. (A2) and (A7), we obtain

$$g^2_{mn,\mu\nu,\mathbf{k}}(\mathbf{R}_p) = N_e^2 N_p^2 \sum_{\mathbf{q}} e^{-i\mathbf{q}\cdot\mathbf{R}_p}\partial V^*_\mu(\mathbf{q})\,\partial V_\nu(\mathbf{q})\,|\langle u_{m\mathbf{k}+\mathbf{q}}|u_{n\mathbf{k}}\rangle|^2. \tag{A8}$$

Now we observe that (i) the largest nonvanishing Fourier component $\mathbf{q}$ in Eq. (A6) corresponds to a small fraction of the Brillouin-zone size, since the phonon perturbation in the Wannier representation is localized within a distance corresponding to a few lattice constants. (ii) For small $\mathbf{q}$, the overlap term $|\langle u_{m\mathbf{k}+\mathbf{q}}|u_{n\mathbf{k}}\rangle|^2$ has no linear variation in $\mathbf{q}$, as can be derived from $\mathbf{k}\cdot\mathbf{p}$ perturbation theory.[88] As a consequence, $|\langle u_{m\mathbf{k}+\mathbf{q}}|u_{n\mathbf{k}}\rangle|^2$ is a slowly varying function of $\mathbf{q}$ in the region of reciprocal space where the ionic term is most significant. The result is that the spatial decay of the squared e-ph matrix element in the phonon Wannier representation [Eq. (A2)] is dominated by the localization of the phonon perturbation. This property allows an efficient interpolation in Bloch space through Eq. (A3).

It should be pointed out that in this derivation, we did not make use of the electron Wannier representation. This constitutes the main difference with the strategy outlined in Sec. III. The advantage of the formulation introduced in Ref. 35 and described in this appendix is that the interpolation over the phonon momentum $\mathbf{q}$ can be performed independently of the electronic momentum and without resorting to electronic Wannier functions. The disadvantage is that when we need to interpolate both on the electronic momentum $\mathbf{k}$ and the phonon momentum $\mathbf{q}$, there is a large computational overhead arising from the need to perform the two operations sequentially. Ultimately, the choice between the two procedures will depend on the specific problem under consideration. When it is hard to obtain electron Wannier functions (e.g., for high-energy conduction band states) or the interpolation over the electron momentum is not needed, it may be preferable to use the scheme outlined in this appendix. In all other cases, the formulation of Sec. III is preferable.

*giustino@civet.berkeley.edu

[1] J. R. Schrieffer, *Theory of Superconductivity* (Benjamin, New York, 1964).

[2] W. Kohn, Phys. Rev. Lett. **2**, 393 (1959).

[3] R. E. Peierls, *Quantum Theory of Solids* (Clarendon, Oxford, 1964).

[4] E. M. Conwell, Proc. Natl. Acad. Sci. U.S.A. **22**, 8795 (2005).

[5] A. Lanzara, P. V. Bogdanov, X. J. Zhou, S. A. Kellar, D. L. Feng, E. D. Lu, T. Yoshida, H. Eisaki, A. Fujimori, K. Kishio, J.-I. Shimoyama, T. Noda, S. Uchida, Z. Hussain, and Z. X. Shen, Nature (London) **412**, 510 (2001).

[6] A. Damascelli, Z. Hussain, and Z.-X. Shen, Rev. Mod. Phys. **75**, 473 (2003).

[7] M. Lazzeri, S. Piscanec, F. Mauri, A. C. Ferrari, and J. Robertson, Phys. Rev. Lett. **95**, 236802 (2005).

[8] N. F. Mott, Proc. Phys. Soc. London **46**, 680 (1934), and references therein.

[9] H. Fröhlich, Phys. Rev. **79**, 845 (1950).

[10] T. Holstein, Ann. Phys. (N.Y.) **8**, 325 (1959).

[11] J. Bardeen and D. Pines, Phys. Rev. **99**, 1140 (1955).

[12] G. Grimvall, *The Electron-Phonon Interaction in Metals* (North-Holland, New York, 1981).

[13] T. K. Mitra, A. Chatterjee, and S. Mukhopadhyay, Phys. Rep. **153**, 91 (1987); *Polarons in Ionic Crystals and Polar Semiconductors*, edited by J. Devreese (North-Holland, Amsterdam, (1972).

[14] G. D. Mahan, *Many-Particle Physics* (Plenum, New York, 1981).

[15] M. Berciu, Phys. Rev. Lett. **97**, 036402 (2006).

[16] P. B. Allen, M. L. Cohen, L. M. Falicov, and R. V. Kasowski, Phys. Rev. Lett. **21**, 1794 (1968).

[17] M. M. Dacorogna, M. L. Cohen, and P. K. Lam, Phys. Rev. Lett. **55**, 837 (1985).

[18] P. K. Lam, M. M. Dacorogna, and M. L. Cohen, Phys. Rev. B **34**, 5065 (1986).

[19] S. Y. Savrasov, D. Y. Savrasov, and O. K. Andersen, Phys. Rev. Lett. **72**, 372 (1994).

[20] S. Y. Savrasov and O. K. Andersen, Phys. Rev. Lett. **77**, 4430 (1996).

[21] S. Y. Savrasov and D. Y. Savrasov, Phys. Rev. B **54**, 16487 (1996).

[22] R. Bauer, A. Schmid, P. Pavone, and D. Strauch, Phys. Rev. B **57**, 11276 (1998).

[23] H. J. Choi, D. Roundy, H. Sun, M. L. Cohen, and S. G. Louie, Nature (London) **418**, 758 (2002).

[24] H. J. Choi, M. L. Cohen, and S. G. Louie, Phys. Rev. B **73**, 104520 (2006).

[25] A. B. Migdal, Zh. Eksp. Teor. Fiz. **34**, 1438 (1958) [Sov. Phys. JETP **7**, 996 (1958)].

[26] P. B. Allen and B. Mikovic, in *Solid State Physics*, edited by H. Ehrenreich, F. Seitz, and D. Turnbull (Academic, New York, 1982), Vol. 32, p. 1.

[27] D. Connétable, V. Timoshevskii, B. Masenelli1, J. Beille, J. Marcus, B. Barbara, A. M. Saitta, G.-M. Rignanese, P. Mélinon, S. Yamanaka, and X. Blase, Phys. Rev. Lett. **91**, 247001 (2003).

[28] X. Blase, Ch. Adessi, and D. Connétable, Phys. Rev. Lett. **93**, 237004 (2004).

[29] M. J. Verstraete and Xavier Gonze, Phys. Rev. B **74**, 153408 (2006).

[30] D. Kasinathan, K. Koepernik, J. Kunes, H. Rosner, and W. E. Pickett, Physica C **460**, 133 (2007).

[31] M. A. L. Marques, M. Lüders, N. N. Lathiotakis, G. Profeta, A. Floris, L. Fast, A. Continenza, E. K. U. Gross, and S. Massidda, Phys. Rev. B **72**, 024546 (2005).

[32] S. Baroni, S. de Gironcoli, A. Dal Corso, and P. Giannozzi, Rev. Mod. Phys. **73**, 515 (2001).

[33] E. A. Ekimov, V. A. Sidorov, E. D. Bauer, N. N. Mel'nik, N. J. Curro, J. D. Thompson, and S. M. Stishov, Nature (London) **428**, 542 (2004).

[34] Y. Takano, M. Nagao, I. Sakaguchi, M. Tachiki, T. Hatano, K. Kobayashi, H. Umezawa, and H. Kawarada, Appl. Phys. Lett. **85**, 2851 (2004).

[35] F. Giustino, Jonathan R. Yates, I. Souza, M. L. Cohen, and S. G. Louie, Phys. Rev. Lett. **98**, 047005 (2007).

[36] K. W. Lee and W. E. Pickett, Phys. Rev. Lett. **93**, 237003 (2004).

[37] L. Boeri, J. Kortus, and O. K. Andersen, Phys. Rev. Lett. **93**, 237002 (2004).

[38] S. Engelsberg and J. R. Schrieffer, Phys. Rev. **131**, 993 (1963).

[39] The spin variable is not shown explicitly since we consider here spin-unpolarized systems. The extension of the present formalism to include spin-dependent electron-phonon interaction does not pose any problems.

[40] M. S. Hybertsen and S. G. Louie, Phys. Rev. B **34**, 5390 (1986).

[41] F. Giustino, M. L. Cohen, and S. G. Louie (unpublished).

[42] L. Hedin and S. Lundqvist, in *Solid State Physics*, edited by F. Seitz, D. Turnbull, and H. Ehrenreich (Academic, New York, 1969), Vol. 23, p. 1.

[43] P. B. Allen, Phys. Rev. B **6**, 2577 (1972).

[44] W. L. McMillan, Phys. Rev. **167**, 331 (1968).

[45] D. Kasinathan, J. Kunes, A. Lazicki, H. Rosner, C. S. Yoo, R. T. Scalettar, and W. E. Pickett, Phys. Rev. Lett. **96**, 047004 (2006).

[46] M. Calandra and F. Mauri, Phys. Rev. B **71**, 064501 (2005).

[47] M. Lüders, M. A. L. Marques, N. N. Lathiotakis, A. Floris, G. Profeta, L. Fast, A. Continenza, S. Massidda, and E. K. U. Gross, Phys. Rev. B **72**, 024545 (2005).

[48] G. H. Wannier, Phys. Rev. **52**, 191 (1937).

[49] N. Marzari and D. Vanderbilt, Phys. Rev. B **56**, 12847 (1997).

[50] R. D. King-Smith and D. Vanderbilt, Phys. Rev. B **47**, 1651 (1993).

[51] R. Resta, Rev. Mod. Phys. **66**, 899 (1994).

[52] L. He and D. Vanderbilt, Phys. Rev. Lett. **86**, 5341 (2001).

[53] I. Souza, N. Marzari, and D. Vanderbilt, Phys. Rev. B **65**, 035109 (2001).

[54] A. Calzolari, N. Marzari, I. Souza, and M. B. Nardelli, Phys. Rev. B **69**, 035108 (2004).

[55] W. Kohn, Phys. Rev. B **7**, 2285 (1973).

[56] F. Giustino and A. Pasquarello, Phys. Rev. Lett. **96**, 216403 (2006).

[57] Since the dynamical matrix is Hermitian, the eigenmodes satisfy the following relation: $\mathbf{e}^{\nu}_{-\mathbf{q}\kappa}=[\mathbf{e}^{\nu}_{\mathbf{q}\kappa}]^{\star}$.

[58] X. Gonze and C. Lee, Phys. Rev. B **55**, 10355 (1997).

[59] M. Born and K. Huang, *Dynamical Theory of Crystal Lattices* (Oxford University Press, Oxford, England, 1954).

[60] S. Barišić, J. Labbé, and J. Friedel, Phys. Rev. Lett. **25**, 919 (1970); L. Pietronero, S. Strässler, and H. R. Zeller, and M. J. Rice, Phys. Rev. B **22**, 904 (1980).

[61] P. Hohenberg and W. Kohn, Phys. Rev. **136**, B864 (1964).

[62] W. Kohn and L. J. Sham, Phys. Rev. **140**, A1133 (1965).

[63] J. Ihm, A. Zunger, and M. L. Cohen, J. Phys. C **12**, 4409 (1979).

[64] A. Mostofi, J. R. Yates, N. Marzari, I. Souza, and D. Vanderbilt, http://www.wannier.org/

[65] X. Wang, J. R. Yates, I. Souza, and D. Vanderbilt, Phys. Rev. B **74**, 195118 (2006).

[66] J. R. Yates, X. Wang, D. Vanderbilt, and I. Souza, Phys. Rev. B **75**, 195121 (2007).

[67] P. K. Lam and M. L. Cohen, Phys. Rev. B **25**, 6139 (1982).

[68] E. Merzbacher, *Quantum Mechanics*, 2nd ed. (Wiley, New York, 1970).

[69] A. A. Maradudin and S. H. Vosko, Rev. Mod. Phys. **40**, 1 (1968).

[70] N. Troullier and J. L. Martins, Phys. Rev. B **43**, 1993 (1991).

[71] D. Vanderbilt, Phys. Rev. B **41**, 7892 (1990).

[72] D. M. Ceperley and B. J. Alder, Phys. Rev. Lett. **45**, 566 (1980).

[73] J. P. Perdew and A. Zunger, Phys. Rev. B **23**, 5048 (1981).

[74] M. Fuchs and M. Scheffler, Comput. Phys. Commun. **119**, 67 (1999).

[75] S. Baroni, A. Dal Corso, S. de Gironcoli, P. Giannozzi, C. Cavazzoni, G. Ballabio, S. Scandolo, G. Chiarotti, P. Focher, A. Pasquarello, K. Laasonen, A. Trave, R. Car, N. Marzari, and A. Kokalj, http://www.pwscf.org/

[76] M. L. Cohen, Phys. Scr., T **T1**, 5 (1982).

[77] M. Methfessel and A. T. Paxton, Phys. Rev. B **40**, 3616 (1989).

[78] M. Hoesch, T. Fukuda, T. Takenouchi, J. P. Sutter, S. Tsutsui, A. Q. R. Baron, M. Nagao, Y. Takano, H. Kawarada, and J. Mizu, Phys. Rev. B **75**, 140508 (2007).

[79] J. Kulda, H. Kainzmaier, D. Strauch, B. Dorner, M. Lorenzen, and M. Krisch, Phys. Rev. B **66**, 241202(R) (2002).

[80] J. Jiang, R. Saito, Ge. G. Samsonidze, S. G. Chou, A. Jorio, G. Dresselhaus, and M. S. Dresselhaus, Phys. Rev. B **72**, 235408 (2005).

[81] W. Kohn, Phys. Rev. Lett. **76**, 3168 (1996).

[82] If we assume that a total-energy minimization within a linear-response computer code requires 1 min on a modern supercomputer and consider that B-doped diamond in the virtual crystal approximation has six phonon modes for every **q** point, we would need $1\times 6\times 50^3$ min to peform the calculations, corresponding to approximately 1 year and 5 months.

[83] T. Yokoya, T. Nakamura, T. Matsushita, T. Muro, Y. Takano, M. Nagao, T. Takenouchi, H. Kawarada, and T. Oguchi, Nature (London) **438**, 647 (2005).

[84] Y. Ma, J. S. Tse, T. Cui, D. D. Klug, L. Zhang, Y. Xie, Y. Niu, and G. Zou, Phys. Rev. B **72**, 014306 (2005).

[85] P. B. Allen and R. C. Dynes, Phys. Rev. B **12**, 905 (1975).

[86] H. J. Xiang, Z. Li, J. Yang, J. G. Hou, and Q. Zhu, Phys. Rev. B **70**, 212504 (2004).

[87] J. Appel and W. Kohn, Phys. Rev. B **4**, 2162 (1971).

[88] P. Y. Yu and M. Cardona, *Fundamentals of Semiconductors: Physics and Material Properties*, 2nd ed. (Springer-Verlag, Berlin, 1999).